Surface displacements and source parameters of the 2003 Bam (Iran) earthquake from Envisat advanced synthetic aperture radar imagery

Gareth J. Funning,[1] Barry Parsons, and Tim J. Wright

Centre for the Observation and Modeling of Earthquakes and Tectonics, Department of Earth Sciences, University of Oxford, Oxford, UK

James A. Jackson

Centre for the Observation and Modeling of Earthquakes and Tectonics, Department of Earth Sciences, University of Cambridge, Cambridge, UK

Eric J. Fielding[2]

Jet Propulsion Laboratory, California Institute of Technology, Pasadena, California, USA

[1] The M_w 6.6, 26 December 2003 Bam (Iran) earthquake was one of the first earthquakes for which Envisat advanced synthetic aperture radar (ASAR) data were available. Using interferograms and azimuth offsets from ascending and descending tracks, we construct a three-dimensional displacement field of the deformation due to the earthquake. Elastic dislocation modeling shows that the observed deformation pattern cannot be explained by slip on a single planar fault, which significantly underestimates eastward and upward motions SE of Bam. We find that the deformation pattern observed can be best explained by slip on two subparallel faults. Eighty-five percent of moment release occurred on a previously unknown strike-slip fault running into the center of Bam, with peak slip of over 2 m occurring at a depth of $\sim$5 km. The remainder occurred as a combination of strike-slip and thrusting motion on a southward extension of the previously mapped Bam Fault $\sim$5 km to the east.

Citation: Funning, G. J., B. Parsons, T. J. Wright, J. A. Jackson, and E. J. Fielding (2005), Surface displacements and source parameters of the 2003 Bam (Iran) earthquake from Envisat advanced synthetic aperture radar imagery, *J. Geophys. Res.*, *110*, B09406, doi:10.1029/2004JB003338.

1. Introduction

[2] Active deformation in Iran is a result of the convergence between the Arabian and Eurasian plates. Recent global plate models, constrained by GPS observations, show approximately north-south shortening in eastern Iran, with rates about 20 mm/yr at 50°E and 26 mm/yr at 60°E [*Sella et al.*, 2002], somewhat less than the rates from older plate models [*DeMets et al.*, 1994; *Chu and Gordon*, 1998]. Arabia-Eurasia convergence is accommodated by deformation in the Zagros in the south and the Alborz and Kopeh Dagh in the north (Figure 1). Central Iran, which lies between these zones of deformation therefore moves northward relative to Eurasia and hence relative to Afghanistan which is attached to the Eurasian plate. The rate of this motion is estimated from recent GPS measurements to be 12–14 mm/yr [*Vernant et al.*, 2004]. The resulting right-lateral shear in eastern Iran is taken up on two north-south strike-slip fault systems located on each side of the aseismic Dasht-e Lut (Figure 1).

[3] On 26 December 2003, an M_w $\sim$6.6 earthquake devastated the town of Bam, destroying over 50% of its buildings. Bam is situated within the Nayband-Gowk-Sabzevaran (NGS) fault system, the western of the strike-slip fault systems bordering the Lut desert. The motion on the NGS system has been estimated at 1–2 mm/yr [*Walker and Jackson*, 2002]. The Gowk Fault, lying 50 km to the northwest of Bam (Figure 2), has been especially active in recent years, with four major earthquakes between 1981 and 1998 [*Berberian et al.*, 1984; *Berberian and Qorashi*, 1994; *Berberian et al.*, 2001]. Bam lies on a prominent splay of the NGS fault system, the Bam Fault, a structure with minor topographic expression but clearly visible in satellite images (Figure 3).

[4] Somewhat surprisingly, preliminary fieldwork and remote sensing studies, particularly evidence from interferometry using Envisat radar data [*Talebian et al.*, 2004], and

---

[1]Now at Berkeley Seismological Laboratory, University of California, Berkeley, California, USA.

[2]Also at Centre for the Observation and Modeling of Earthquakes and Tectonics, Department of Earth Sciences, University of Cambridge, Cambridge, UK.
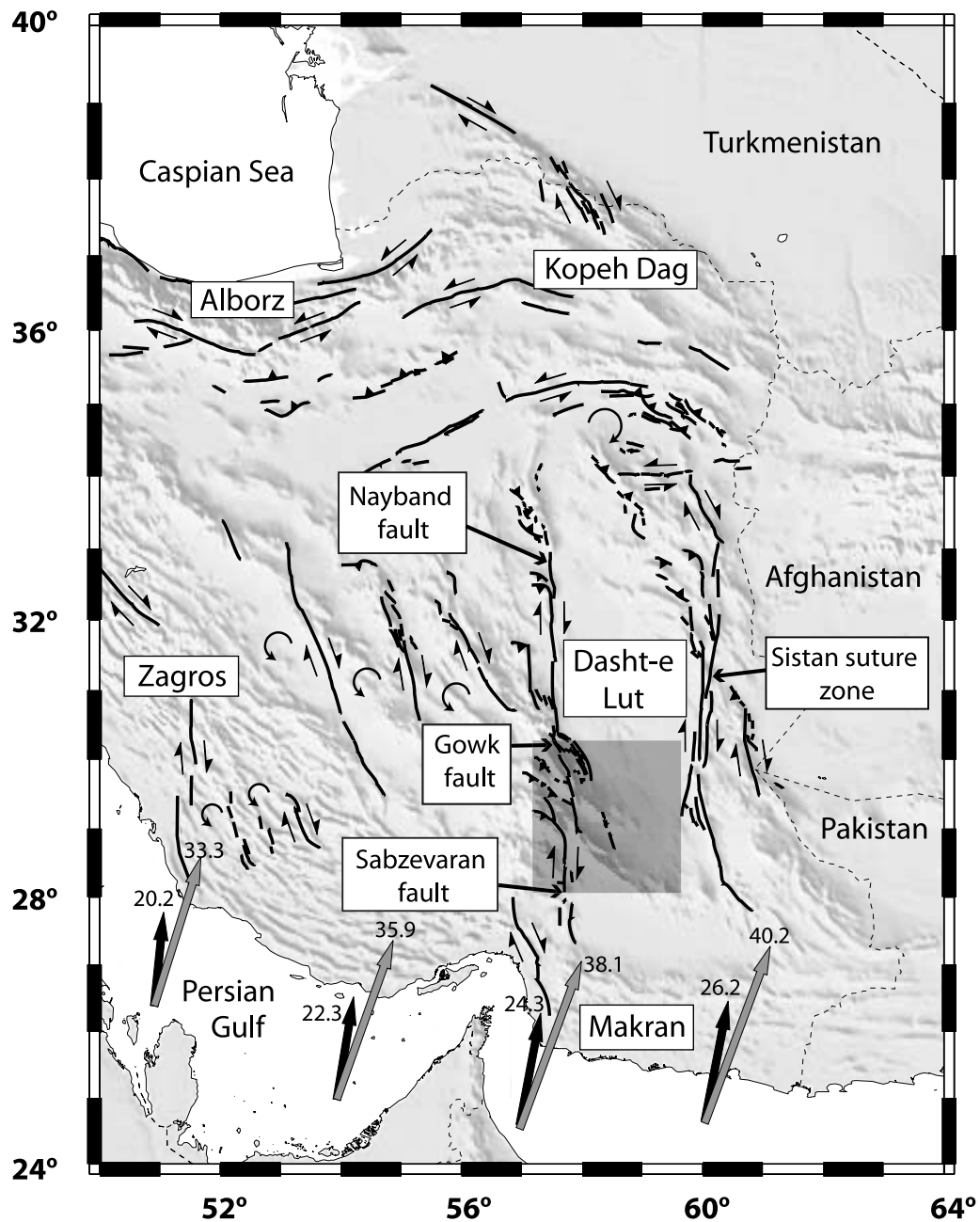
Figure 1. Shaded relief map of central and eastern Iran showing major faults. Arabia-Eurasia relative plate motions are shown as the black and gray arrows, with rates in mm/yr. Black arrows are GPS estimates [*Sella et al.*, 2002], and gray arrows are 3 Ma average rates based on seafloor magnetic anomalies estimated using Africa-Eurasia [*Chu and Gordon*, 1998] and Arabia-Africa [*DeMets et al.*, 1994] motions. Shaded area shows the location of Figure 2 around Bam.

also aftershock locations [*Tatar et al.*, 2004], indicated that the earthquake main shock occurred not on the previously mapped Bam fault, but on a hitherto unknown blind fault extending ~12 km southward from the center of the city. There is evidence to suggest that the Bam fault may have moved as a secondary event in the earthquake, however. Small-scale fissuring was observed in the vicinity of the Bam fault [*Talebian et al.*, 2004], and there are features in broadband teleseismic waveform data from stations to the east of the earthquake that can not be explained by a single strike-slip source [*Talebian et al.*, 2004; J. A. Jackson et al., manuscript in preparation, 2005].

[5] In this paper, we analyze synthetic aperture radar (SAR) interferograms derived from Envisat radar data. Use of interferograms from both ascending and descending satellite passes enables us to separate the effects of the main and secondary events. Combining the interferometry with subpixel matching of the SAR amplitude images allows us to obtain the full three-dimensional displacement field for the earthquake, distinguishing vertical from horizontal
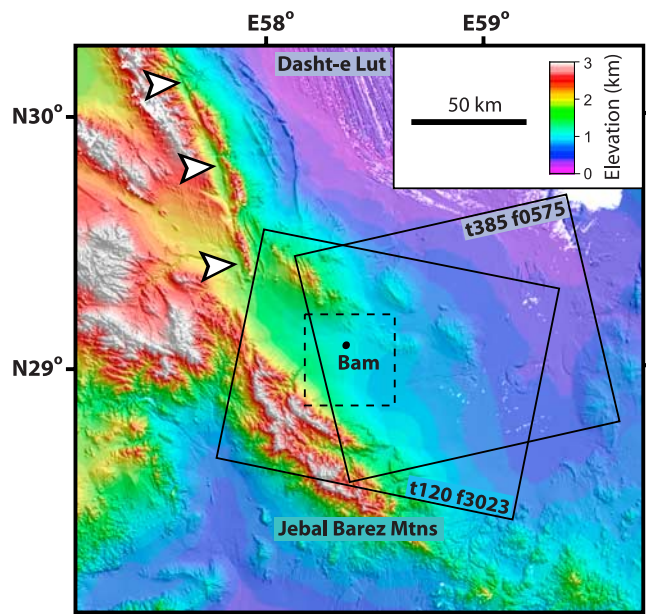
Figure 2. Shaded relief topography and elevation of the region surrounding Bam. Data shown are 3 arc sec data from the Shuttle Radar Topography Mission. Topography is illuminated by a light source to the NE at an inclination of 45°. The Gowk fault, the nearest segment of the through-going Nayband-Gowk-Sabzevaran system bordering the western edge of the Dasht-e Lut (labeled), and a center of recent seismicity, is delineated by white arrowheads. The Jebal Barez mountains, the main topographic feature near Bam (location marked) are labeled. (Solid lines indicate Envisat ASAR image frames covering the epicentral region of the earthquake (track and frame numbers are given). Dashed box represents the 40 × 40 km area around Bam shown in subsequent figures.)

motions. With these observations, the secondary event can be shown to have had a significant thrust component, probably occurring on the mapped Bam fault and triggered by the main strike-slip earthquake.

2. Obtaining Displacements From Envisat ASAR Imagery

2.1. Interferometric Data

[6] SAR interferometry (InSAR) is a precise space geodetic technique that allows the remote mapping of continental deformation at high (∼40 m) spatial resolution [*Massonnet and Feigl*, 1998; *Bürgmann et al.*, 2000]. It is especially effective in unvegetated, arid areas, where the effects of temporal decorrelation are minimal [*Berberian et al.*, 2001; *Fialko et al.*, 2001], conditions that exist in the area surrounding Bam, which is located in the southwestern corner of the Dasht-e Lut, a 500 km wide desert region of eastern Iran.

[7] The Bam earthquake was one of the first earthquakes for which a preseismic archive of images acquired by the advanced synthetic aperture radar (ASAR) instrument on Envisat, a C band radar with 5.6 cm wavelength, was available. The epicentral area was covered by recent acquis-
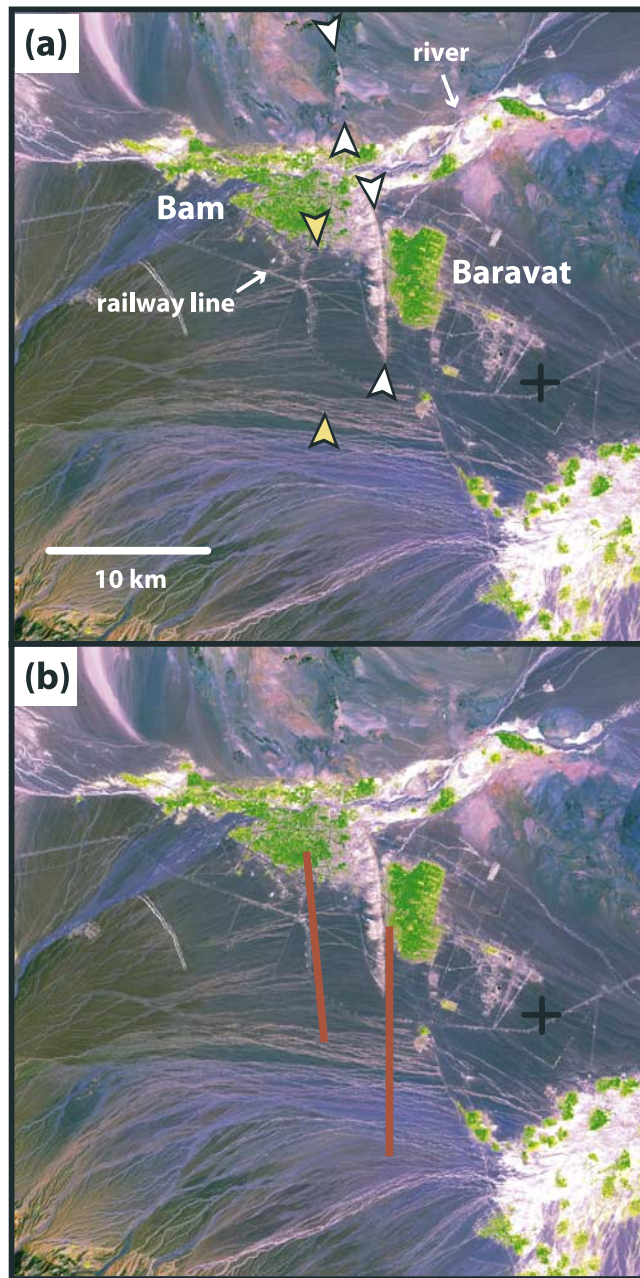

Figure 3. LANDSAT-ETM 541 false color image of the epicentral area of the Bam earthquake, acquired 10 January 1999. Green colors indicate the presence of vegetation in Bam and Baravat, important regional producers of dates. Black cross is located at 29°N, 58.5°E for reference, as in following figures. (a) Main faults in the area, as mapped in the field. Yellow arrowheads show the extents of the mapped main surface rupture due to the earthquake [*Talebian et al.*, 2004]. Note that there are no surface features through which a fault may be recognized; the only recognizable feature in the vicinity is a railway line (labeled). White arrowheads show two segments of the Bam fault, a prominent ridge running between Bam and Baravat (labeled), and to the north of the Posht-rud river. (b) Locations of our best fitting two-fault model, projected updip to the surface (red lines).

Table 1.   Details of Interferograms Constructed for This Study

	Track	Frame	θ_i[a]	Azimuth[b]	Date 1	Date 2	Δt, d^{-1}	$B_\perp$,[c] m^{-1}	h_a,[d] m^{-1}
Ascending	385	0575	23°	348.1°	16 Nov 2003	25 Jan 2004	70	50	260
Descending	120	3023	23°	191.5°	3 Dec 2003	11 Feb 2004	70	4	3250

[a]Incidence angle of radar at scene center.
[b]Orientation of the satellite track direction, clockwise from north.
[c]Perpendicular baseline.
[d]Altitude of ambiguity.

itions on both ascending and descending tracks (Figure 2). We selected and then processed, using the Jet Propulsion Laboratory/California Institute of Technology ROI_PAC software [*Rosen et al.*, 2004], two coseismic pairs of images, one from an ascending track and the other from a descending track, with favorable perpendicular baselines and short temporal separations (Table 1). A 3 arc sec digital elevation model (DEM) from the Shuttle Radar Topography Mission (SRTM) [*Farr and Kobrick*, 2000] was used to correct for topographic artifacts and geocode the interferograms. The ~7 m vertical uncertainty in SRTM data is considerably smaller than the altitudes of ambiguity for both interferograms (Table 1), and consequently, any remaining topographic signal in the interferograms will be negligible. Any residual phases in the far field, away from the earthquake, are likely to be due to differences in tropospheric water vapor levels between the acquisitions.

[8] The wrapped and unwrapped interferograms are shown in Figures 4a–4d. The interferometric correlation (a measure of the stability of the phase contribution due to the distribution of small radar scatterers within each interferogram pixel, and therefore a measure of the degree of change to the ground surface) is mostly very high in both interferograms (Figures 4e–4f), in keeping with the environmental conditions. There are localized areas of decorrelation, the largest being in the city of Bam and neighboring town of Baravat, where there is significant vegetation (shown as green in Figure 3) and also extensive damage to buildings as a result of the earthquake. In addition, a band running to the south of Bam also shows low correlation, corresponding to the earthquake surface rupture [*Talebian et al.*, 2004; *Fielding et al.*, 2005]. The deformation signals are asymmetric in both interferograms, with the majority of deformation occurring to the west of the fault surface rupture in the ascending track interferogram, and to the east of the fault in the descending track interferogram. In both cases, the peak deformation occurs at the southern end of the fault. Any residual orbital tilts and offsets remaining in the data after processing have been removed by subtracting a plane fitted to the data in the far field, away from the deformation signal. The root-mean-square (RMS) misfit between the data and this plane in the far-field, of the order of 5 mm for both interferograms, is representative of the low level of atmospheric noise in each image, and is used as an estimate for the uncertainty in the data (Table 2).

2.2. Azimuth Offsets

[9] Subpixel matching of SAR amplitude images is an established technique for obtaining additional horizontal displacement information for earthquakes [*Michel et al.*, 1999; *Peltzer et al.*, 1999; *Jónsson et al.*, 2002]. Azimuth offsets are the positional shifts necessary to align SAR amplitude pixels in the azimuth (along-track) direction for a pair of SAR images, and therefore contain information about ground displacements resolved into the along-track direction. We calculate azimuth offsets for both coseismic pairs of SAR images used to calculate interferograms (Table 1). Offsets were measured from the full-resolution single-look complex (SLC) images at 4 pixel intervals, and the signal improved by masking out large pixel offsets ($\geq$0.5 pixels), median filtering, averaging in the azimuth direction, and removing trends and offsets using the far-field data, as for the interferogram data. However, a significant degree of noise remains in the data; the uncertainty in these measurements, estimated by calculating the misfit between the data and a best fitting plane in the far field, is of the order of 11–12 cm (Table 2).

[10] Our calculated displacements are given in Figure 5. The peak-to-trough displacement measured here is of the order of 1 m, with the maximum motion either side of the fault located ~1800 m away from the fault. Since the maximum deformation did not occur at the fault, this indicates that the maximum slip on the fault must have occurred at a few kilometers depth, rather than at the surface. The deformation signal drops away strongly with distance either side of the fault; at distances of 20 km or more, the deformation is obscured by the noise in the data. The pattern of displacements is consistent with a large component of right-lateral strike-slip motion.

2.3. Constructing a Deformation Field in Three Dimensions

[11] With three or more independent observations of ground displacement from different viewing geometries, it is possible to construct a three-dimensional model of the deformation which occurred in an earthquake [*Fialko et al.*, 2001; *Wright et al.*, 2004b]. The combination of ascending and descending track interferometric phase, sensitive to vertical and east-west motion, and azimuth offsets, sensitive to north-south motion, is particularly well suited to this purpose.

[12] To solve for a three-dimensional displacement field, we invert the observations at each pixel using a least squares method, weighting each data set by the inverse of its far-field variance [*Wright et al.*, 2004b]. As the azimuth offset data only contain data with a high signal-to-noise ratio within 20 km of the fault, we resample all four data sets onto the same 100 × 100 grid with a pixel spacing of 400 m. Further details of the inversion method are given in Appendix A.

[13] The calculated three-dimensional displacement field is shown in Figure 6. The pattern of deformation is asymmetric in the x (east) and z (up) components with both showing more motion to the east of the surface rupture than to the west. The y (north) component, almost parallel to the
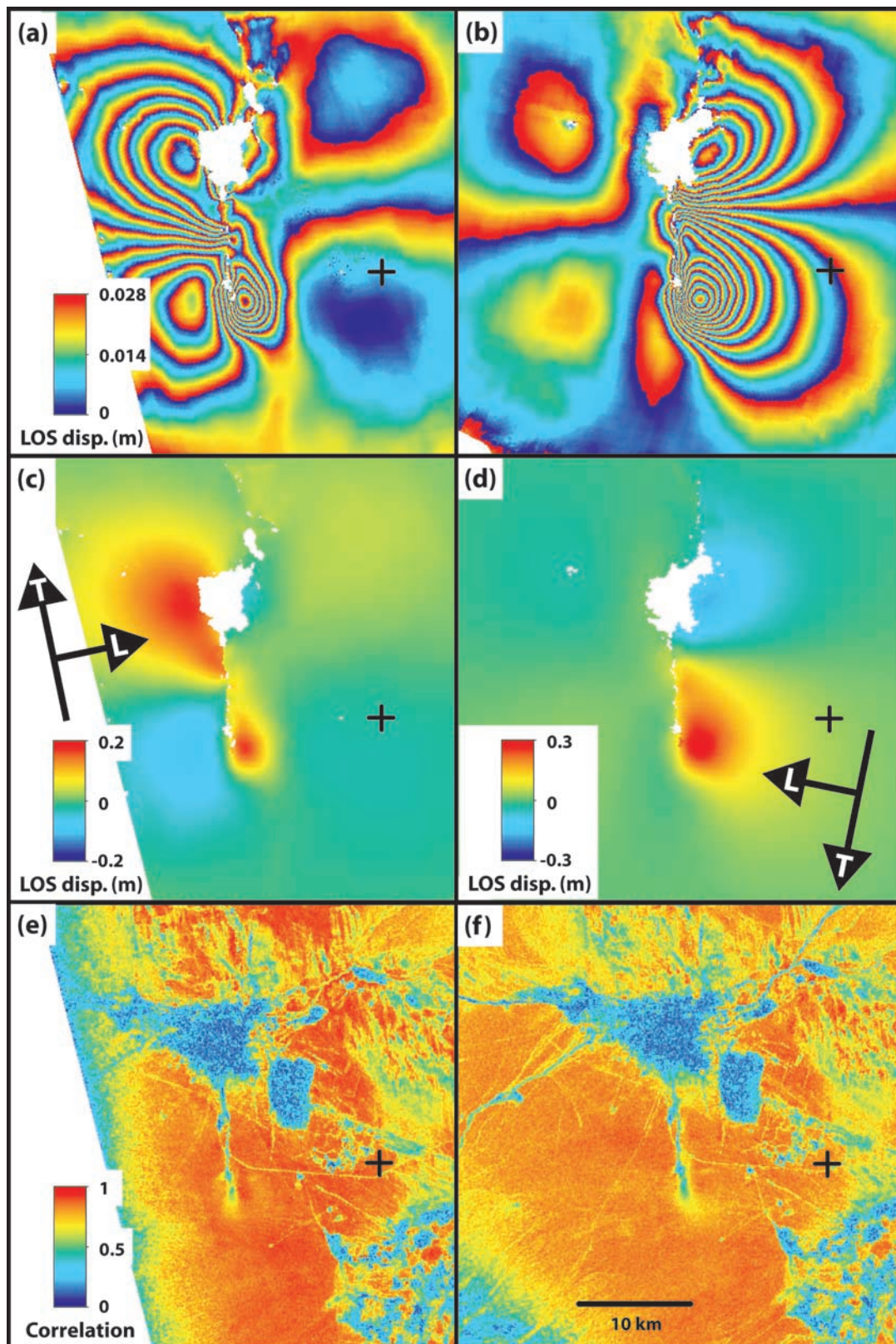
Figure 4. Interferometric data used in this study. Line-of-sight (LOS) displacements shown use the convention that positive motion is toward the satellite. (a) Detail of wrapped ascending (track 385) interferogram of the Bam earthquake. (b) Wrapped descending (track 120) interferogram. (c) Unwrapped ascending interferogram. (d) Unwrapped descending interferogram. (e) Correlation of ascending track interferogram. (f) Correlation of descending track interferogram. Area is as defined in Figure 2. Black arrows indicate directions of satellite track (T) and LOS vector (L).

Table 2. Properties of Displacement Data Sets

	Pointing Vector (East, North, Up)	Far-Field RMS, m
Ascending interferogram	−0.3225, −0.0680, 0.9441[a]	0.004
Descending interferogram	0.4009, −0.0816, 0.9125[a]	0.005
Ascending azimuth offsets	−0.2060, 0.9790, 0[b]	0.114
Descending azimuth offsets	−0.1940, −0.9810, 0[b]	0.117

[a]From the ground to the satellite, calculated at the center of the surface rupture.
[b]Along the satellite track.

surface rupture, has the largest signal, with peak deformation occurring approximately 2 km either side of the fault rupture, suggesting that the earthquake involved predominantly right-lateral strike-slip motion, and that more slip occurred at depth than at the surface. We estimate the 1σ errors in the x, y and z components to be 0.9, 8.9, and 0.8 cm, respectively. The larger errors in the y component are due to the high sensitivity of the noisy azimuth offset data to N-S motions; the more precise InSAR data are relatively insensitive to motions in a N-S direction, and therefore have only a small effect on the estimated precision of the motion in this direction.

3. Elastic Dislocation Modeling of Displacement Data

3.1. Single Fault Models

[14] The asymmetric pattern of deformation observed in both interferograms is consistent with predominantly right-lateral strike-slip motion on a subvertical fault. To illustrate this point, we calculate displacements for a simple vertical fault model (fault parameters are strike 180°, dip 90°, rake 180°, slip 1.8 m, length 12 km, top depth 0.6 km, bottom depth 13 km), assuming that the fault may be represented as a rectangular dislocation in an elastic half-space [Okada, 1985]. Our model displacements are shown in Figure 7a. As expected for a vertical N-S dislocation pinned at its ends, the pattern of deformation is symmetric about the fault in the x component and antisymmetric in the y and z components. As in our estimated three-dimensional displacement field (Figure 6), the majority of motion occurs in the y component, with lesser components of x and z motion near the ends of the fault.

[15] Because a N-S fault forms a very acute angle with the satellite track for both the ascending and descending tracks (Table 1), little of the fault-parallel north-south motion contributes to the line-of-sight (LOS) displacement measured by the satellite, compared with the east-west and vertical components. This is demonstrated in Figure 7b, where the model displacements of Figure 6 are scaled by their respective LOS pointing vector components for both ascending and descending interferograms (Table 2), giving their contribution to the total LOS displacement. In both cases, the y component has the smallest contribution to LOS displacement, despite having the largest amplitude of the three components. The pattern of displacements observed in the total LOS displacements for both ascending and descending interferograms depends, then, on the interaction
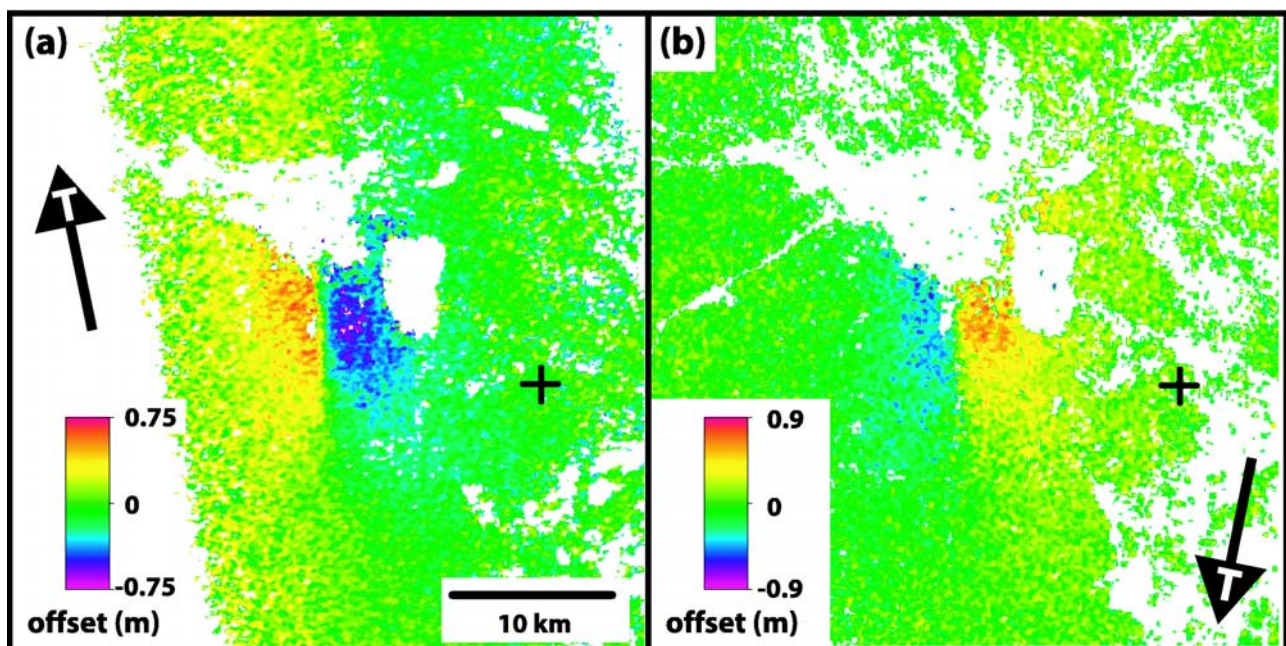

Figure 5. Azimuth offset data used in this study. (a) Azimuth offsets for the ascending track data. (b) Azimuth offsets for the descending track data. Black arrows indicate satellite track direction in which these offsets are measured.
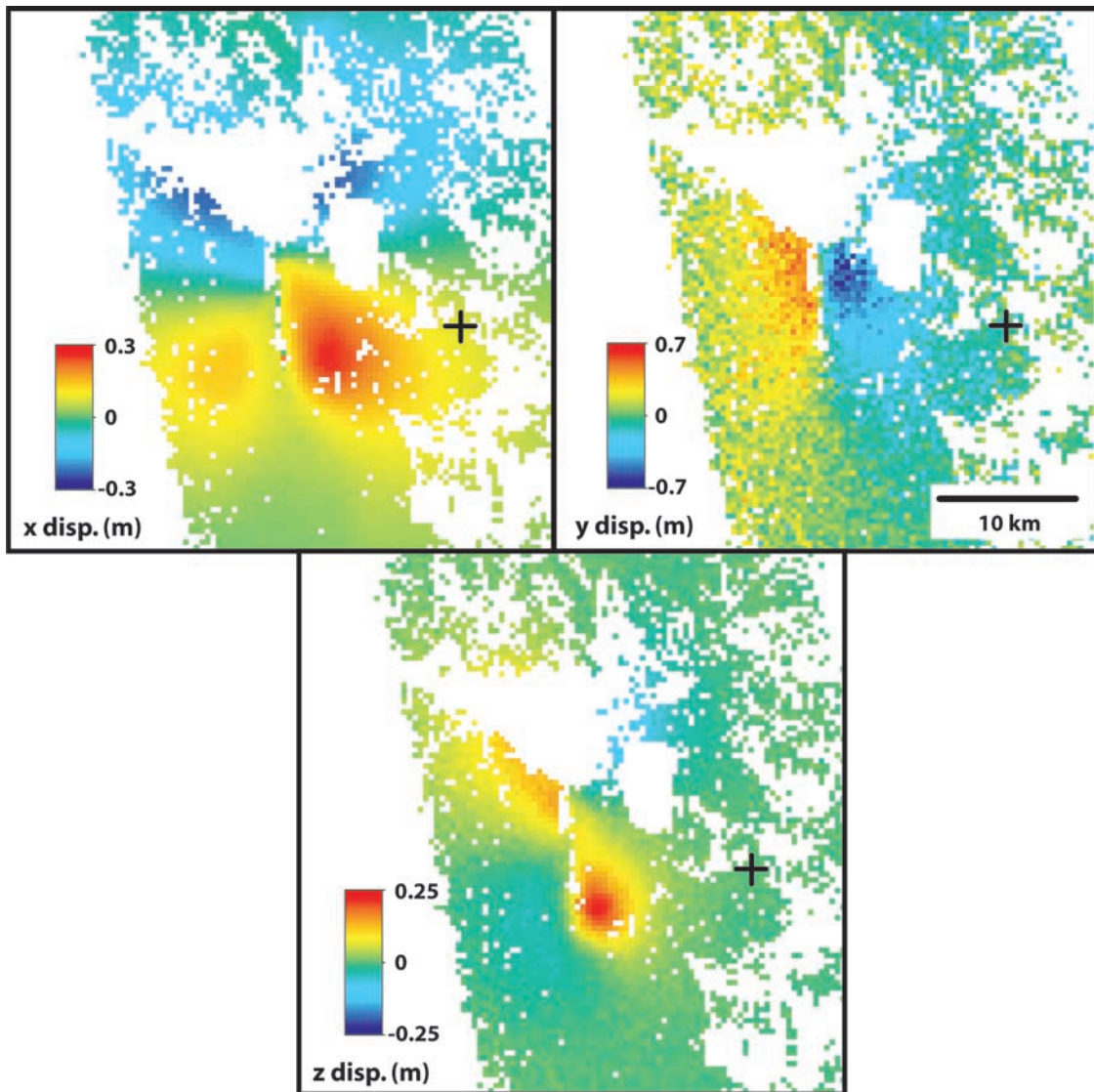
Figure 6. The 3-D displacement field for the Bam earthquake from inverting displacement data. East (x), north (y), and up (z) components are shown.

between the approximately equal *x* and *z* contributions to LOS displacement. These components sum constructively on the west side of the fault in the ascending case and the east side in the descending case, and destructively on the east side of the fault in the ascending case and the west side in the descending case. The result in each case is a highly asymmetric deformation pattern with the majority of LOS displacement occurring on one side of the fault, similar to that observed (Figure 4).

[16] To solve for the configuration of fault parameters that best describe the observed deformation, we first resample the data to expedite this process. At this preliminary stage, we do not use the noisier azimuth offset data, which if downweighted according to their level of noise would provide only a weak constraint on the solution; indeed, inversion tests using all of the displacement data give results that do not differ significantly from those obtained from the interferogram data alone. These interferogram data are sampled at a 400 m spacing within 7 km of the fault, a

1000 m spacing within 15 km of the fault, and at a spacing of 5000 m elsewhere, reducing the data set from ∼2 million data points to ∼4000. Then, modeling the fault again as a rectangular dislocation in an elastic half-space [*Okada*, 1985], we employ a downhill simplex algorithm with multiple Monte Carlo restarts [*Clarke et al.*, 1997; *Wright et al.*, 1999] to manipulate the fault model until a configuration of parameters corresponding to a global minimum misfit to the resampled data is found. Our best fitting model parameters are listed in Table 3. The 1σ uncertainties given for these parameters were estimated using a Monte Carlo error estimation technique (Appendix B) [*Wright et al.*, 2003; T. J. Wright et al., manuscript in preparation, 2005]. The uncertainties in the model, in general, are very small, presumably due to the excellent degree of data coverage, right up to the fault on both sides, and the low level of atmospheric noise in the data. Trade-offs between model parameters, also estimated by this technique, are also small; the most important (i.e., the trade-offs between fault slip,
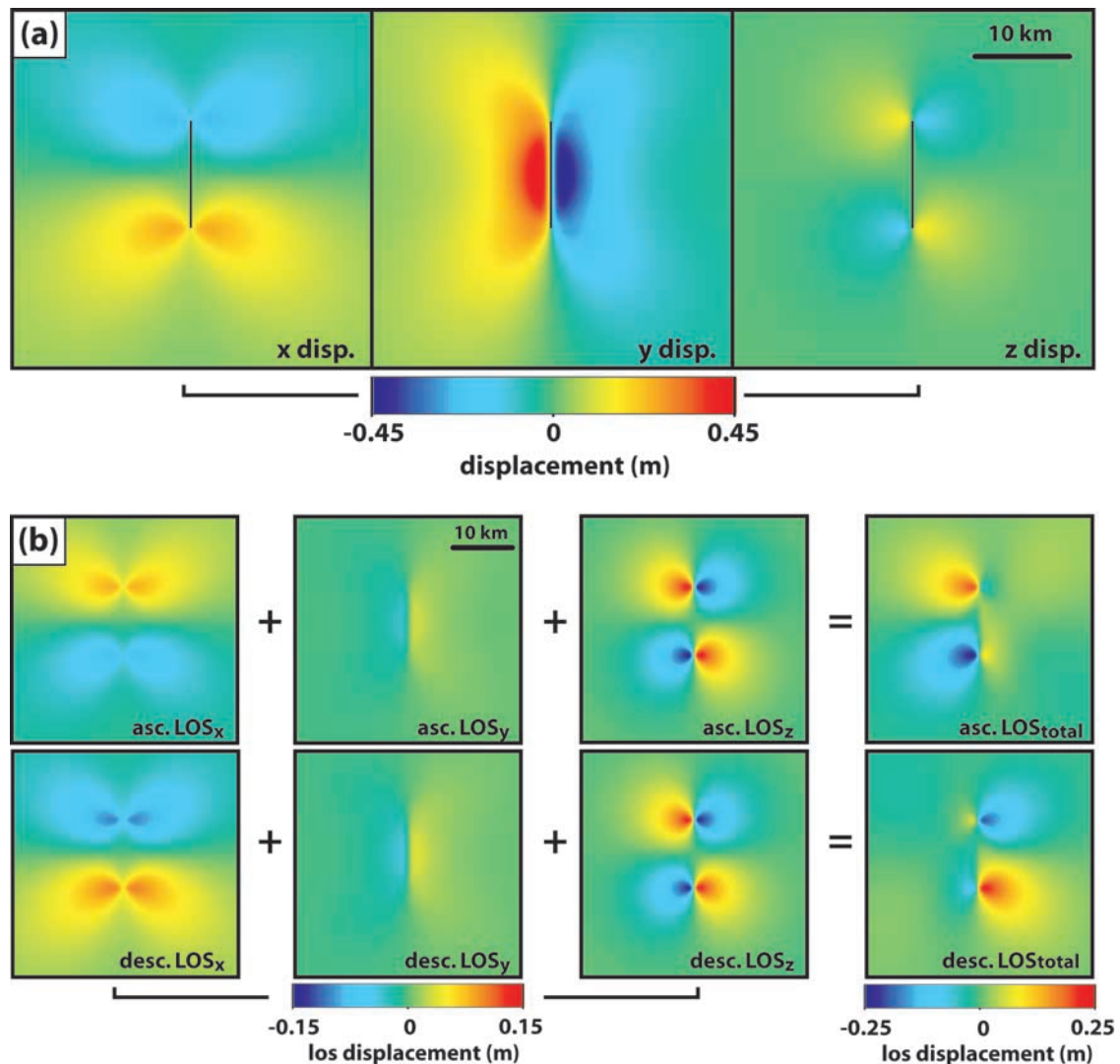
Figure 7. Single fault models of the Bam earthquake. (a) Calculated east (x), north (y), and up (z) components of an Okada elastic dislocation model of a vertical strike-slip fault with assumed fault parameters (strike 180°, dip 90°, rake 180°, slip 1.8 m, length 12 km, top depth 0.6 km, bottom depth 13 km). (b) The same displacements scaled by their LOS pointing vector components in both ascending and descending viewing geometries and how they sum to give the observed interferograms.

fault width, centroid depth, and moment) involve only around 10% variations in the involved parameters.

[17] We find that uniform slip on a single, near-vertical strike-slip fault leaves large unmodeled residuals in the southeast quadrant of the deformation pattern, the area south of Baravat, for both the ascending and descending data (Figure 8), giving a high RMS misfit of 2.5 cm, close to the deformation of a single interference fringe. Such residuals suggest that the observed pattern of deformation cannot have been the result of motion on a single fault with pure strike-slip motion alone. Indeed, if this were the case, we would have expected the deformation pattern within the interferograms to fully flip to the opposite side with the change of viewing geometry from ascending to descending tracks. In fact, in both the ascending and descending interferograms there is a component of deformation in the southeast quadrant that does not flip (Figure 4). In addition,

detailed comparison between Figures 6 and 7a suggests that a single pure strike-slip fault underestimates the observed deformation here in both x and z components.

[18] The implication is that additional eastward and upward motions are required in this area to explain these differences between the ascending and descending interferograms. One means through which such motions could be achieved is by increasing the amount of thrust motion at the southern end of the fault, through a change of rake. We tested this hypothesis by solving for variable slip and variable rake on an extended fault plane. Assuming the fault geometry found in the uniform slip inversion, we extend the fault plane along strike and downdip to give a length of 24 km and width of 20 km, and divide this into a series of 1 × 1 km patches. We then solve for the best fitting values of strike-slip and dip-slip motion for each fault patch in a least squares sense, employing Laplacian smoothing to

Table 3. Source Parameters of the Bam Earthquake From Seismology and Elastic Dislocation Modeling

	Number of Faults	Latitude, deg	Longitude, deg	Depth,[a] km	Strike	Dip	Rake	Slip, m	Length, km	Width, km	M_0, ×10^18 N m	RMS, m
Seismological Solutions												
Harvard CMT	1	29.100	58.240	15.0	172°	59°	167°	—	—	—	9.3	—
NEIC	1	29.010	58.266	14.0	174°	88°	178°	—	—	—	6.6	—
Talebian et al. [2004]	2	28.972[b]	58.294[b]	6.0	357°	88°	−166°	—	—	—	7.6	—
		28.864	58.294	5.0	180°	30°	90°	—	—	—	1.5	—
This Study												
Uniform slip	1	29.037 ± 0.001[c]	58.353 ± 0.001[c]	5.2 ± 0.1	354.4 ± 0.2°	83.8 ± 0.3°	−177.6 ± 0.1°	2.20 ± 0.04	12.0 ± 0.1	8.1 ± 0.3	7.3 ± 0.2	0.025
Variable slip and rake	1	29.040[c]	58.356[c]	8.1	354.6 ± 0.2°	83.8°	variable	2.58[d]	22[e]	19[e]	13.8	0.019
Uniform slip	2	29.038 ± 0.001[c]	58.357 ± 0.001[c]	5.5 ± 0.1	354.6 ± 0.2°	85.5 ± 0.3°	−177.8 ± 0.2°	2.14 ± 0.03	12.0 ± 0.1	8.6 ± 0.3	7.6 ± 0.2	0.017
		28.988 ± 0.002[c]	58.406[c]	6.7 ± 0.1	180.0°	63.9 ± 1.3°	149.5 ± 2.4°	2.04 ± 0.52	14.8 ± 0.2	1.4 ± 0.3	1.4 ± 0.1	
Variable slip	2	29.040[c]	58.356[c]	6.4	354.6[c]	85.5°	−177.8°	2.69[d]	20[e]	15[e]	9.1	0.013
		28.988[c]	58.406[c]	5.9	180.0°	63.9°	149.5°	2.04[d]	18[e]	6[e]	1.6	

[a]Centroid depth.
[b]Fixed to location in the EHB catalog [*Engdahl et al.*, 1998] provided by E. R. Engdahl (personal communication, 2004).
[c]Center of the fault plane projected updip to the surface.
[d]Peak slip.
[e]Dimensions of area enclosed by the slip contour within which 95% of fault slip occurred.

prevent unphysical oscillatory slip. Further details of this inversion method are given in Appendix C.

[19] The resulting model, along with synthetic and residual interferograms, is plotted in Figure 9, with details of the solution given in Table 3. The slip pattern (Figure 9e) shows one major asperity, with peak slip of ~2.6 m at 5 km depth. At the southern end of the asperity, in the upper 5 km of the fault, there is a small thrust component to the displacement, creating an additional component of upward motion as may have been anticipated from the three-dimensional (3-D) pattern of displacements (Figure 6). Overall, there is an improvement in the fit to the data over the uniform slip case, as evidenced by a reduction in the RMS misfit to 1.9 cm; however substantial residuals, up to four interference fringes, still remain at the southern end of the fault. In particular, there are elongate residuals to the east of the fault in both residual interferograms (Figures 9c and 9d). Similar models where vertical or steep westward dips are assumed show a worsened fit to the data. We therefore conclude that slip on a single planar fault cannot explain the observed deformation.

[20] An alternative means of increasing the eastward and upward motions in the southeast quadrant would be through secondary slip on a westward dipping fault located further to the east, with a significant component of thrust motion. Such a model would be consistent with body wave seismic observations for this event [*Talebian et al.*, 2004; J. A. Jackson et al., manuscript in preparation, 2005].

3.2. Two Fault Models

[21] If the observed deformation pattern for the Bam earthquake is due to slip on two faults, one problem that arises in the modeling is the separation of the signal from each fault from the total deformation observed. The deformation patterns due to two subparallel faults less than 10 km apart will overlap, meaning that attempts to model the fault geometries simultaneously will lead to trade-offs between fault parameters in inversion solutions. Our initial attempts to solve for the geometries of both faults simultaneously, using the simplex algorithm method mentioned above, failed to converge to a global minimum misfit, presumably due to the effects of such trade-offs; smaller misfits were obtained when one of the faults was fixed with assumed fault parameters.

[22] In order to narrow the range of possible two fault solutions, we performed a parameter search for the dip and rake of both faults, modelled as uniform slip rectangular dislocations as for the single fault case above, solving for the depth extents and slip of both faults and holding strike and location fixed. The possibility of the two faults intersecting was prevented by setting appropriate lower bounds on the depth of the secondary fault. A number of different surface locations of the secondary fault were tried. By selecting the configuration of fault dips and rakes that give the lowest misfit to the data (main fault parameters are dip 84°, rake −175°; secondary fault parameters are dip 55°, rake 150°), we obtained a first-pass model for the parameters of the two faults, which we then used as the starting point for an iterative process to find a best fitting two fault solution.

[23] Holding each fault fixed in turn, we solved, as above, for the best fitting parameters of the other fault with
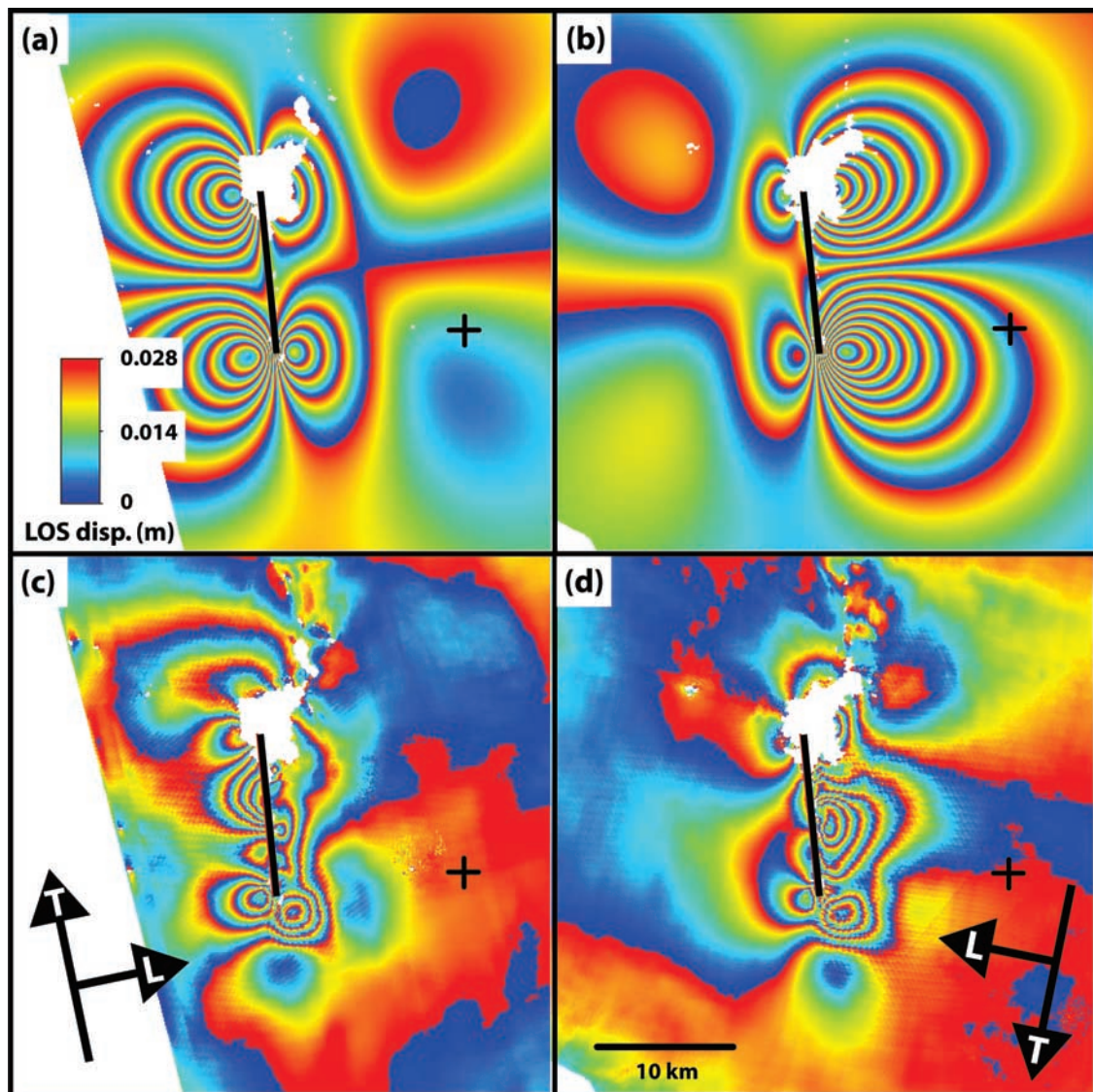
Figure 8. Best fitting single fault uniform slip model of the Bam earthquake. (a) Model ascending interferogram. (b) Model descending interferogram. (c) Residual ascending interferogram. (d) Residual descending interferogram. Black lines show location of the fault when projected updip to the surface.

all parameters free, repeating until the model had converged on a minimum misfit solution. As for the parameter search, the fault geometries were constrained so that the faults were not permitted to crosscut each other. The final two-fault uniform slip model that we obtain is listed in Table 3, and the predicted and residual fringes are shown in Figure 10. In this model, the optimum location for the secondary fault is close to the location of the previously identified Bam Fault, a prominent feature in satellite images of the area (Figure 3), and an area where minor cracks were observed following the earthquake [*Talebian et al.*, 2004]. The fit to the data is improved over the single fault case, with the reduction in the near field residual fringes (Figures 10c–10d) reflected in the improved RMS misfit of 1.7 cm. The second fault here has a different geometry to that suggested by *Talebian et al.* [2004] on the basis of seismological evidence; the second fault in that case was assumed to be a shallow thrust,

and projected to the surface some 9 km to the east of the main fault, at a location inconsistent with the mapped location of the Bam Fault.

[24] The 1σ uncertainties given for the model parameters were estimated using the same Monte Carlo error estimation technique as used above (section 3.1 and Appendix B). Uncertainties are generally lower for the main fault parameters than for the secondary fault parameters, where there are strong trade-offs between slip and depth, manifest as a correlation between these parameters in the perturbed model results. Again, it was only possible to estimate the uncertainties for each fault in turn, due to the trade-offs between the model parameters of the two faults; therefore these uncertainties are underestimates.

[25] The fit to the InSAR data may be further improved by allowing variations in slip on the fault planes. Using the strikes, dips and rakes of the two faults as determined for
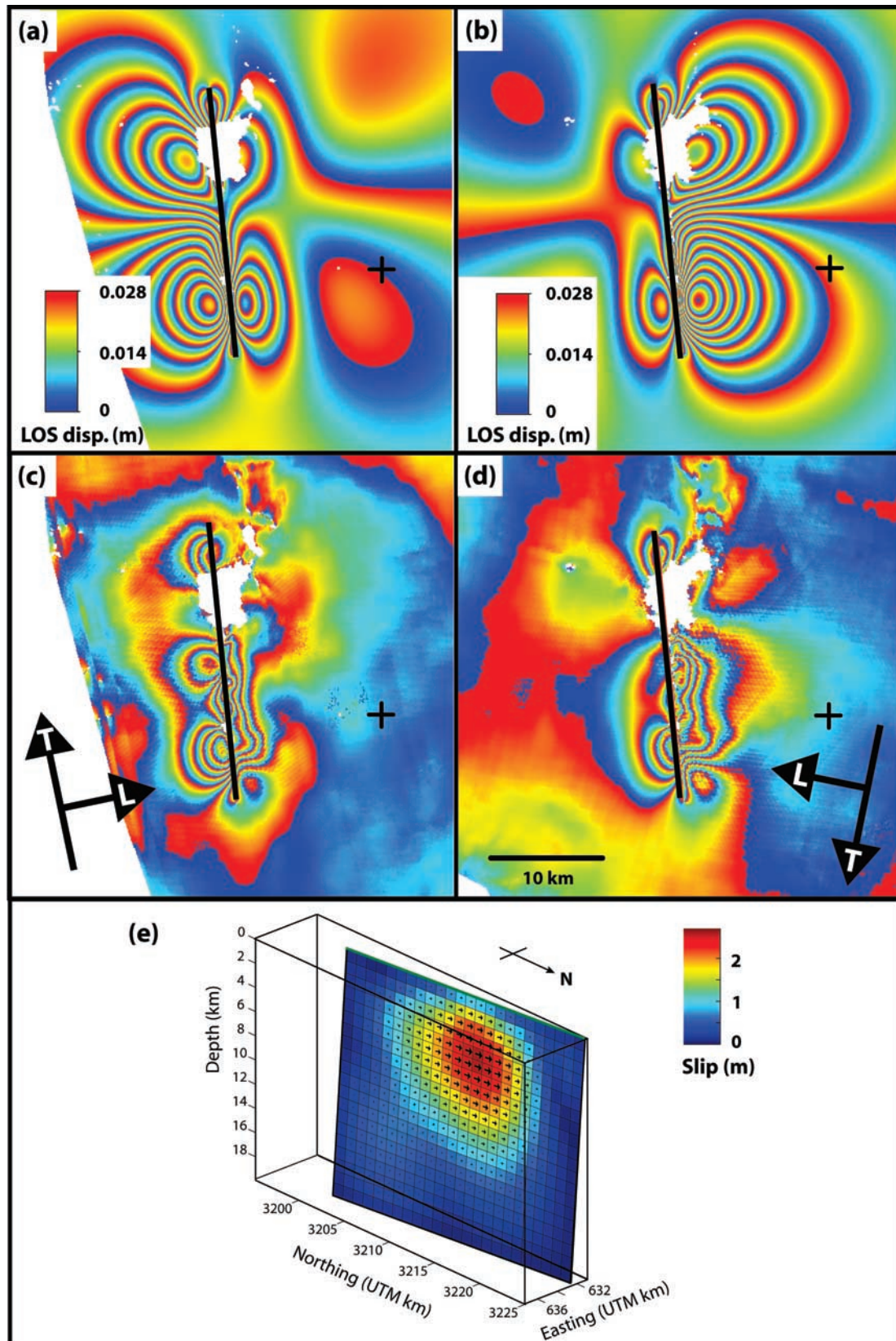
Figure 9. Single fault model with variable slip and rake for the Bam earthquake. (a) Model ascending interferogram. (b) Model descending interferogram. (c) Residual ascending interferogram. (d) Residual descending interferogram. Black lines show location of the fault when projected updip to the surface. (e) Distribution of slip and rake on the fault for this model. Black arrows indicate direction of motion of the footwall of the fault.
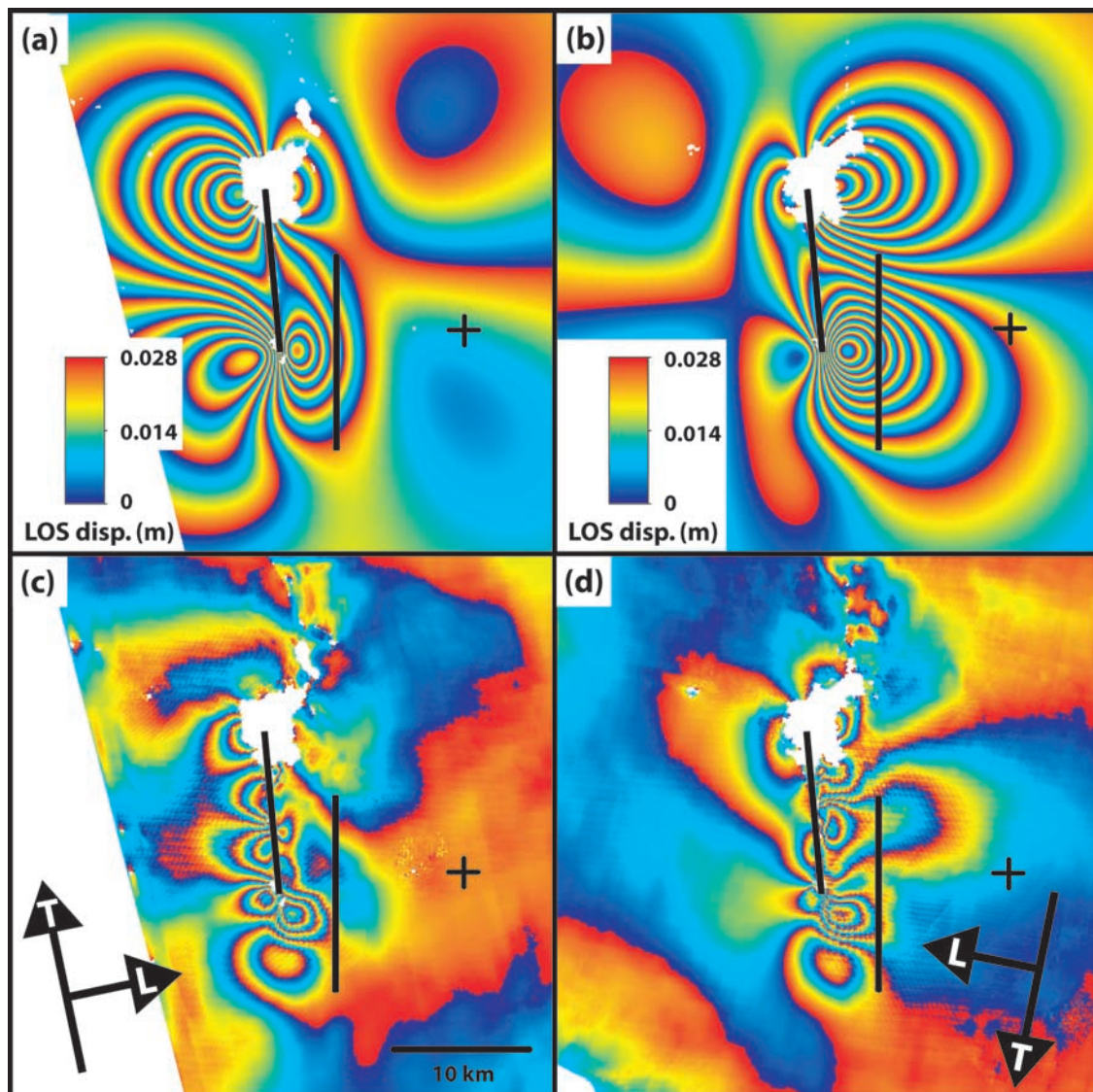
Figure 10. Best fitting two fault uniform slip model of the Bam earthquake. (a) Model ascending interferogram. (b) Model descending interferogram. (c) Residual ascending interferogram. (d) Residual descending interferogram. Black lines show locations of the faults when projected updip to the surface.

the uniform slip case above, we extend the main fault to an along-strike length of 24 km and a downdip width of 20 km, and the secondary fault to 24 km in length and 8 km in width, subdividing each into 1×1 km patches, and solve for the best fitting distribution of slip on those faults in a least squares sense. Again, we impose a Laplacian smoothing condition to prevent unphysical oscillatory slip, and use a nonnegative least squares algorithm to eliminate retrograde motion on the faults. Further details of the inversion are given in Appendix C.

[26] The slip distributions we obtain for the two faults are shown in Figure 11, with model details listed in Table 3. Approximately 85% of the total slip occurred on the main fault in a single contiguous deforming zone, or asperity. As we are using here a homogeneous elastic model (rigidity modulus is 34.3 GPa), this represents the same percentage of the total moment release. Peak model slip on the main fault was 2.7 m at a depth of 5 km; even given a likely

spatial resolution in the model at this depth of ∼5 km (Appendix C, Figure C2a), over 2 m of slip can be resolved here. On the upper kilometer of the fault, slip peaked at 0.8 m. The deforming area on the main fault, defined here as the area enclosed by the slip contour within which 95% of integrated fault slip occurs, is 20 km long and 15 km wide, stretching beneath the center of Bam at its northern end. On the secondary fault, slip is concentrated in two asperities, and occurs further to the south than for the main fault. The deforming area here is 18 km long and 6 km wide, with no significant slip propagating to the surface. The peak slip on the secondary fault is 2.0 m in the northernmost of the two asperities at the base of the fault, close to the area of peak slip on the main fault. Again, given a likely spatial resolution here of ∼4 km (Appendix C, Figure C2a), both of these asperities can be resolved by our model.

[27] In order to assess the quality of this solution, we calculate model (Figure 11) and residual (Figure 12) inter-
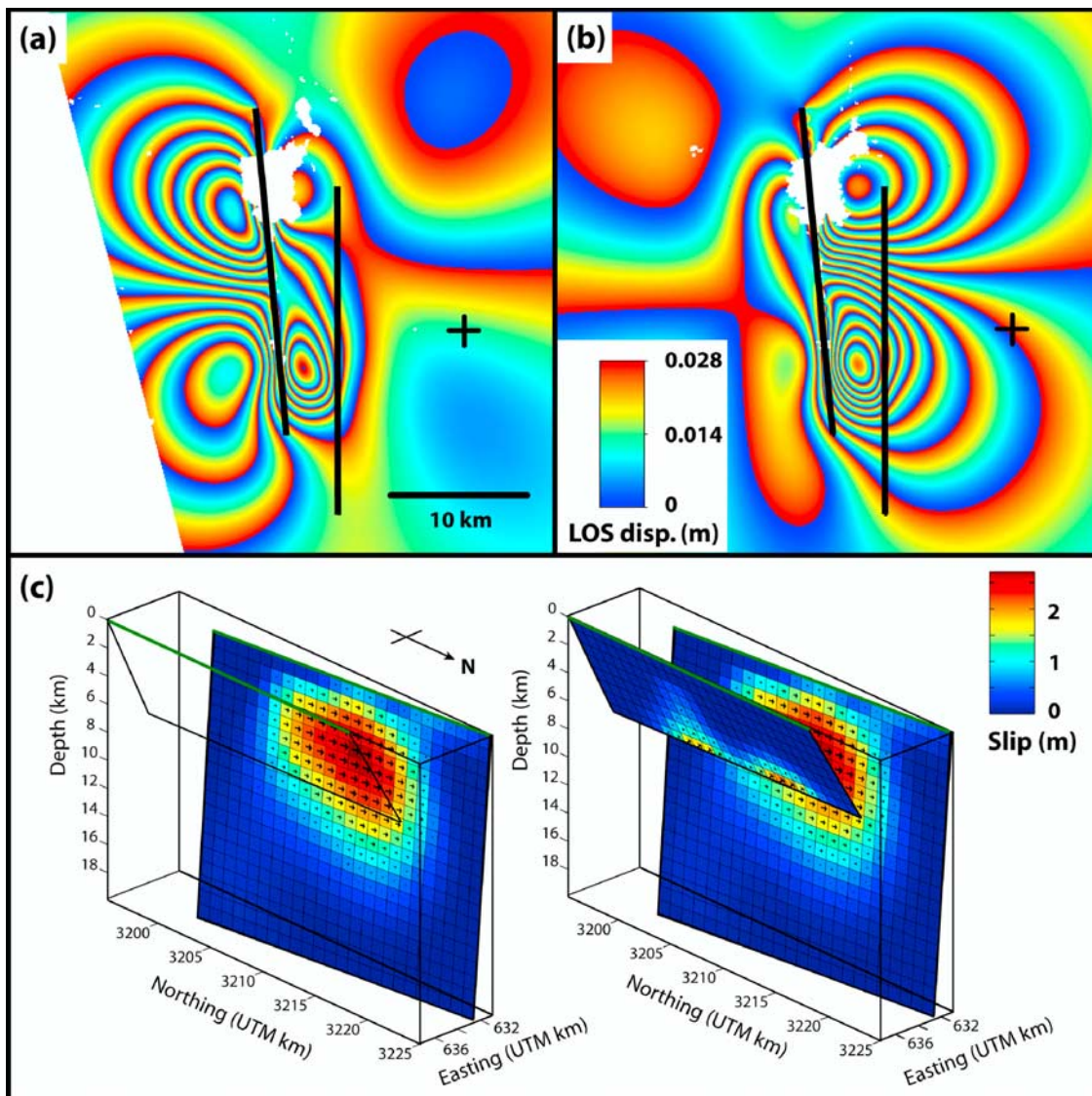
Figure 11. Two fault variable slip model of the Bam earthquake. (a) Model ascending interferogram. (b) Model descending interferogram. Black lines indicate updip projections of the fault planes to the surface. (c) (left) Distribution of slip on the main fault and (right) distribution of slip on both faults. Viewing position is from the NE. Black arrows indicate the direction of motion of the western side of the fault with respect to the east. Green lines indicate updip projections of the fault planes to the surface.

ferograms. We find that the variable slip model reproduces the main features of the observed data. The misfit to the data in the far field is of the order of the estimated uncertainty in the data (Table 2); in the near field some residual fringes remain, centered on the main fault rupture, and are likely to represent unmodeled fault complexity, either in terms of shallow fault segmentation which is observed in the field along the main fault rupture [*Talebian et al.*, 2004] and in high-resolution SAR correlation maps of the area (Figures 4e–4f) [*Fielding et al.*, 2005], or in terms of a reduced rigidity modulus in the shallow subsurface, as inferred for other earthquakes [*Simons et al.*, 2002; *Fialko*, 2004]. The RMS misfit to the InSAR data is 1.3 cm.

[28] To determine the level of uncertainty in our slip estimates, we again perturb our data 100 times using realistic correlated noise, as for the error estimation process for the uniform slip models above (Appendix B) and invert

these data to generate 100 perturbed slip distributions. The standard deviations of the slip on each fault patch, a measure of the uncertainty in each slip estimate, calculated from these perturbed slip distributions, are plotted in Figure 12c. The level of uncertainty is generally low (standard deviation ≤16 cm), presumably due to the low levels of atmospheric noise in the data, and the constraints applied in the inversion process; the largest uncertainties occur at depth on both faults, as might be expected, and in the near-surface fault patches at the northern end of the main fault, which are located in the center of Bam, where building damage and the presence of vegetation have resulted in an incoherent signal in that area in both interferograms (Figure 4).

[29] A final, independent test of the validity of our model can be made by calculating model and residual azimuth offsets (Figure 13), as the azimuth offset data were not used
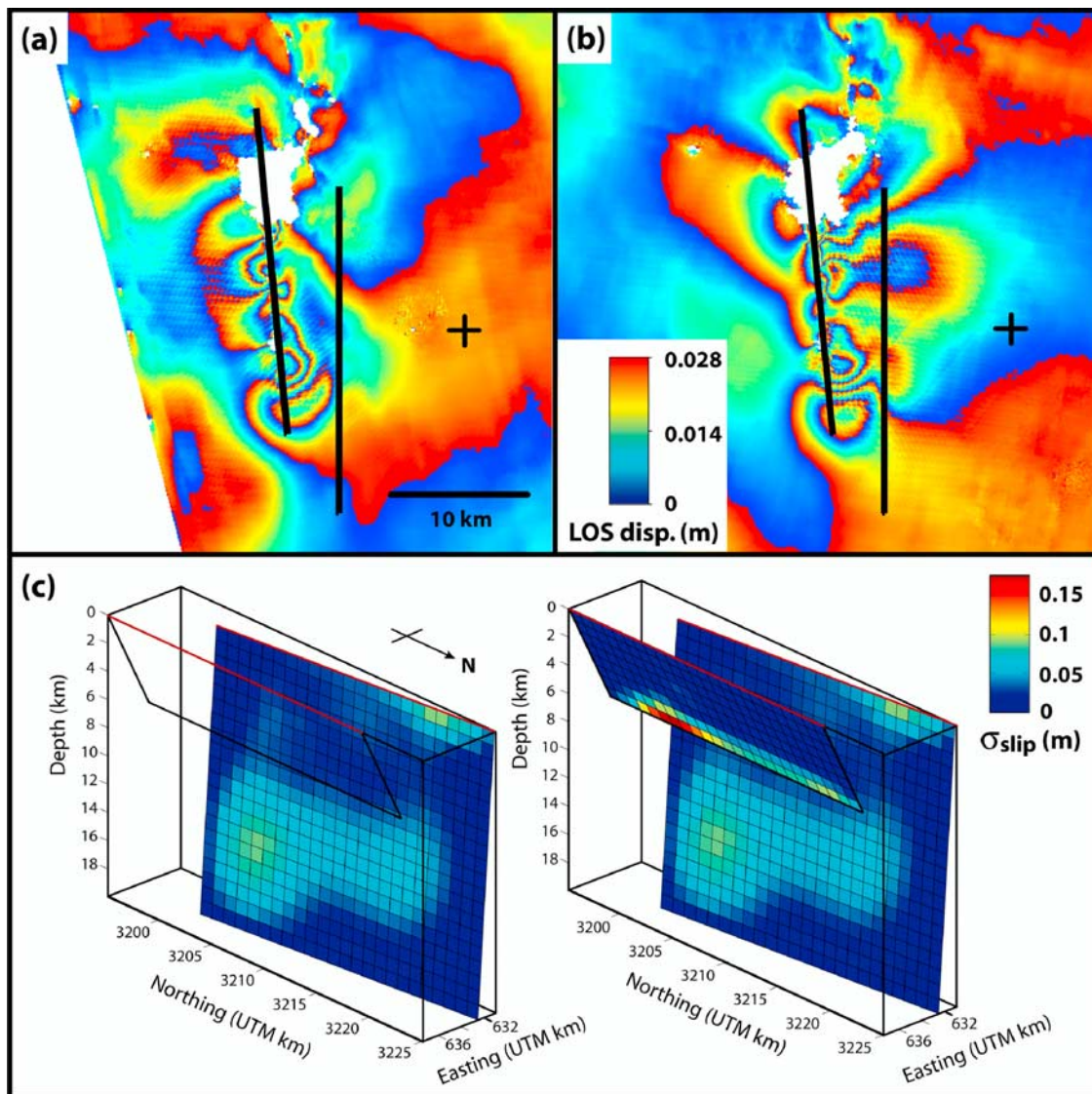
Figure 12. Fit to data and uncertainties of the two fault variable slip model of the Bam earthquake. (a) Residual ascending interferogram. (b) Residual descending interferogram. Black lines indicate updip projections of the fault planes to the surface. (c) (left) Plot of 1σ uncertainties in slip on the main fault and (right) plot of 1σ uncertainties in slip on both faults. Viewing position is from the NE. Red lines indicate updip projections of the fault planes to the surface.

in the inversion. In the far field, any misfit is indistinguishable from the noise in the data; in the near field there are residual displacements along the main fault and in the area of overlap between the two faults immediately SW of Baravat, areas in which the model also misfits the InSAR data. Overall, the RMS misfit to the azimuth offset data is 12.3 cm, close to our estimated uncertainties in those data (Table 2), suggesting that they are consistent with our model. Indeed, when the InSAR and azimuth offset data, sampled using the same scheme, are weighted by the inverse of their far field uncertainties and inverted jointly, there is no significant change to the solution obtained.

4. Discussion

[30] The results of our modeling of the Bam earthquake show that the majority of the fault motion observed by InSAR occurred on two faults, a hitherto hidden, or "blind" strike-slip fault extending under the center of Bam, and a second, obliquely slipping fault whose surface trace is close to the previously mapped Bam Fault, extending further to the south (Figure 3b). The geometry of these two faults, which appear likely to intersect and interact at depth, is similar to that proposed for other recent earthquakes in eastern Iran, as we shall explain below.

4.1. Properties of Faults in the Bam Area

[31] Perhaps the most striking discovery made from InSAR observations of the Bam earthquake is that the majority of the displacement in the event occurred on a fault whose existence was unknown, and unknowable, prior to the earthquake: a blind fault with no surface expression. The absence of geomorphic indicators, such as topographic
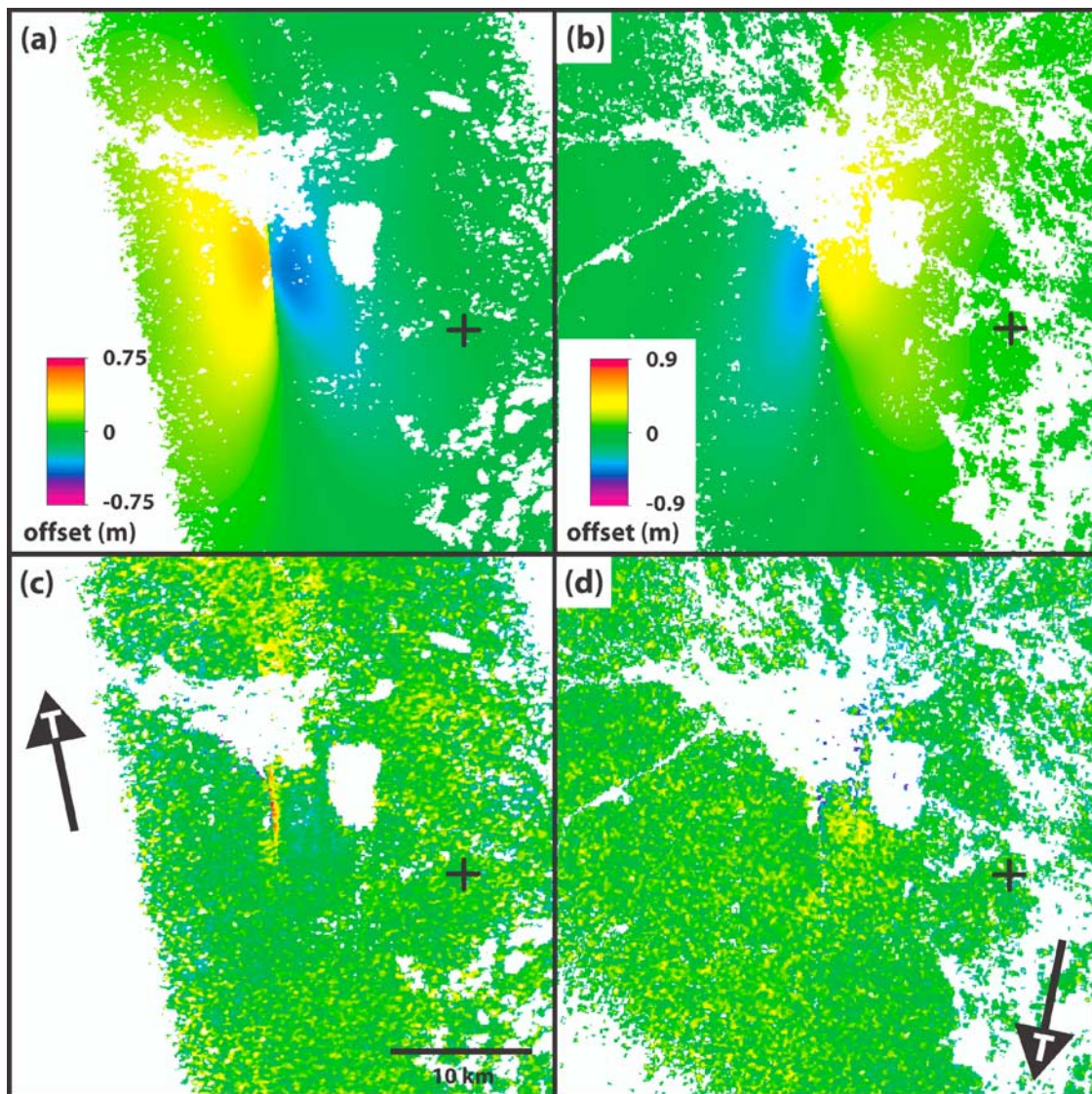
Figure 13. Synthetic azimuth offsets, which provide an independent test of the model, to be compared with the observed data shown in Figure 5. (a) Model ascending azimuth offsets. (b) Model descending azimuth offsets. (c) Residual ascending azimuth offsets. (d) Residual descending azimuth offsets.

features near the fault, or offset drainage channels, can be ascribed to several factors. The lack of a vertical component in the fault motion, as evidenced by the almost pure right-lateral fault rake obtained for the main fault in our source parameter inversion (Table 3), as well as field observations [*Talebian et al.*, 2004], would suggest that the topographic signature due to a single earthquake would be of the order of a few centimeters, and therefore many hundreds of earthquake cycles would be needed to build topography.

[32] The dominant geomorphic feature in the area south of Bam is an alluvial fan system building northeastward from the Jebal Barez Mountains to the SW (Figure 2), and a number of drainage channels from this system can be seen in satellite images of the area (Figure 3). Indeed, several of the drainage channels cut straight across the known location of the main fault without being deflected, suggesting that the growth of the alluvial fans in the area is likely to be both more rapid and of a larger amplitude, than the growth of topography due to motion on the main fault. It seems likely

that the surface effects of an earthquake similar to the 2003 event could be erased by one of the flood events which infrequently inundatate the area, and if the repeat interval of such floods were shorter than the repeat interval of the earthquakes, which may be thousands of years, no evidence of a fault would be preserved at the surface.

[33] In contrast to the main fault, the secondary fault that we model in our inversions does appear to have a long-term surface expression. The surface projection of this fault appears to coincide at its northern end with the location of the mapped Bam Fault, previously identified as a blind reverse fault, active in the late Quaternary [*Berberian*, 1976], which is represented at the surface by a 20 m high ridge running between Bam and Baravat, that is clearly visible in satellite images of the area (Figure 3). Minor cracks were observed at the foot of the ridge in postearthquake field surveys [*Talebian et al.*, 2004]. Aerial photographs of this structure suggest that its continuing southward growth is deflecting several E-W drainage chan-

nels around its southern end (J.A. Jackson, unpublished data, 2004). Our variable slip inversion results support this idea of a southward propagating fault, with the majority of the modelled deformation on the secondary fault occurring on an asperity located to the south of the mapped fault, and therefore show that the fault extends further to the south than its surface features currently suggest. Our results also suggest that although there was a significant component of thrust motion on the fault in the earthquake, consistent with its surface expression, the motion was strongly oblique, with a dominant right-lateral strike-slip component.

[34] The close proximity of the two faults raises the possibility of interactions between the faults at depth. Indeed, the northernmost of the two asperities on the secondary fault is located very close in space to the region of greatest slip on the main fault (Figure 11), suggesting that the motion may have transferred across from the main fault to the secondary fault, or been directly triggered by the motion on the main fault. Broadband body wave seismic studies show that a source model with two subevents with the same strike, dip, rake and moment as our two-fault solution can fit observed seismograms if the subevent on the secondary fault initiated 1 s after that on the main fault (J. A. Jackson et al., manuscript in preparation), offering some support to these ideas.

[35] As well as the possibility of fault triggering, there is also the probability of a degree of transpressive deformation occurring in the region between the two faults, both of which have major right-lateral strike-slip components, as the increased eastward and upward motions in this area suggest (Figure 6). Field observations of the main fault rupture show an increasing degree of vertical offset toward its southern end [Fielding et al., 2005], which, along with the more eastward orientation of the southernmost rupture segment, may reflect the increasing influence of the secondary fault to the southeast.

4.2. Complex Faulting Earthquakes in Eastern Iran

[36] The complex faulting seen in the Bam earthquake has some similarities to patterns of faulting seen in other recent earthquakes in eastern Iran. The 14 March 1998 M_w 6.6 Fandoqa earthquake, the most recent earthquake to occur on the nearby Gowk fault system, around 100 km to the northwest, is one such event. At Fandoqa, the strike-slip faulting motion of the earthquake was accompanied by aseismic movement on the Shahdad thrust, a shallow dipping thrust fault located 30 km to the northeast, which was observed using InSAR [Berberian et al., 2001; Fielding et al., 2004]. In addition, teleseismic studies of an earlier earthquake, the 11 June 1981 M_w 6.6 Golbaf event which ruptured a section of the Gowk fault to the northwest of Fandoqa [Berberian et al., 1984], show that the earthquake is best represented as two subevents on subparallel faults. The first subevent showed oblique slip with a significant thrust component on a west dipping fault, the second and larger subevent strike-slip motion on a subvertical fault located to the west [Berberian et al., 2001], a configuration very similar to that which we find for Bam. Similarly complex fault geometries have been proposed for large earthquakes outside Iran, for instance, the 1957 Gobi-Altay earthquake, where near-simultaneous strike-slip and thrust faulting occurred on parallel faults [Kurushin et al., 1997],

and the 2002 Denali, Alaska, earthquake, where rupture initiated on a thrust fault and subsequently transferred to a neighboring strike-slip fault system [e.g., Eberhart-Phillips et al., 2003; Wright et al., 2004a].

[37] If such complex faulting patterns are commonplace in Iran, then InSAR is an ideal technique with which to identify them. As mentioned above, the desert conditions in eastern Iran tend to result in excellent coherence in SAR interferograms and good results can be obtained for intervals of five years or more. In this study, the combination of the desert conditions and the 70 day interval between acquisitions means that in both interferograms the coherence is very high right up to the faults (Figure 4), allowing the fault locations to be determined to high precision. These factors, along with the approximately N-S orientation of the faults, also meant that it was possible to measure an azimuth offset signal for the Bam earthquake, despite the significant level of noise. With information from both ascending and descending tracks, there was sufficient information to calculate 3-D displacements, a useful tool for our understanding of the faulting in the earthquake. It is clear that short time intervals and both ascending and descending coverage are highly desirable in order to gain the fullest understanding of the complex deformation that may occur in future earthquakes, in Iran or elsewhere.

4.3. Implications for Seismic Hazard

[38] The human history of the city of Bam extends back in time for around 1800 years. Bam has a rich water supply due, most likely, to its proximity to active faults, as seen in other desert areas of Iran, where water is otherwise scarce. Faulting can offset aquifers, creating natural artesian wells which can be exploited by the digging of qanats, water-bearing tunnels. As a result, the city became a stop for Zoroastrian and Muslim pilgrims and a regional center of trade, originally as a staging post for caravans crossing the Dasht-e Lut into Sistan and Baluchistan, and later as a producer of dates and citrus fruits. However, for this whole interval of time, no records exist of any earthquakes in the area [Ambraseys and Melville, 1982]. Without such historical information to determine the repeat interval of earthquakes in the area around Bam, and the added complication that the main fault involved in the Bam earthquake was unknown before the earthquake, it is extremely difficult to estimate future seismic hazard in this area. Paleoseismic trenching of the faults we have identified in our analysis may assist the hazard assessment process and lead to better estimates of earthquake repeat rates in the area around Bam, but until we devise methods for identifying blind strike-slip faults such as that running to the south of Bam, we will not know the threat posed by such structures to other areas.

Appendix A: Inverting for a 3-D Displacement Field

[39] This inversion method is based on that of Wright et al. [2004b], who investigate constructing 3-D displacement fields from a range of different InSAR geometries. The line-of-sight (LOS) vector for a given data set is defined as a unit row vector $\hat{\mathbf{p}}$ (p_x, p_y, p_z), pointing from the ground to the satellite in a local east, north, up reference frame. Values of

p_x, p_y and p_z for each data set are given in Table 2. The observed line-of-sight displacement of the ground, d, defined as positive toward the satellite for InSAR data, and positive along-track for azimuth offsets, is then given by $d = \hat{\mathbf{p}}\mathbf{u}$ where $\mathbf{u}$ is the column vector $(u_x, u_y, u_z)^T$ of the components of displacement in the same reference frame.

[40] For each pixel on the ground there are four observations of displacement, two from InSAR LOS displacements and two from azimuth offsets. We incorporate this information into a column vector $\mathbf{D}$, where $\mathbf{D} = (d_1, d_2, d_3, d_4)$. Then, by analogy with above,

$$\mathbf{D} = \mathbf{P}\mathbf{u}, \tag{A1}$$

where $\mathbf{P}$ is the 4×3 matrix

$$\mathbf{P} = \begin{pmatrix} \hat{\mathbf{p}}_1 \\ \hat{\mathbf{p}}_2 \\ \hat{\mathbf{p}}_3 \\ \hat{\mathbf{p}}_4 \end{pmatrix}. \tag{A2}$$

If $\mathbf{\Sigma_D}$ is a covariance matrix containing the squares of the errors of the respective data sets, which are assumed to be independent, along its leading diagonal, the equation may be weighted by premultiplying both sides by its inverse, i.e.,

$$\mathbf{\Sigma_D^{-1}}\mathbf{D} = \mathbf{\Sigma_D^{-1}}\mathbf{P}\mathbf{u}. \tag{A3}$$

The normal equations for a least squares solution to the weighted formulation are therefore

$$\mathbf{P^T}\mathbf{\Sigma_D^{-1}}\mathbf{D} = \mathbf{P^T}\mathbf{\Sigma_D^{-1}}\mathbf{P}\mathbf{u}, \tag{A4}$$

giving a best fitting solution

$$\bar{\mathbf{u}} = \left[\mathbf{P^T}\mathbf{\Sigma_D^{-1}}\mathbf{P}\right]^{-1}\mathbf{P^T}\mathbf{\Sigma_D^{-1}}\mathbf{D}. \tag{A5}$$

The errors in each component of the 3-D model, σ_x, σ_y, σ_z, which are influenced by the level of noise in each data set and the LOS vector for each data set, are given by the relation

$$\left(\sigma_x^2, \sigma_y^2, \sigma_z^2\right) = diag\left[\mathbf{P^T}\mathbf{\Sigma_D^{-1}}\mathbf{P}\right]^{-1}. \tag{A6}$$

Appendix B: Estimation of Uncertainties and Trade-Offs Using Correlated Noise

[41] In order to estimate uncertainties and trade-offs in our inverse models we use a Monte Carlo technique, where 100 perturbed data sets are created using "realistic" noise, which we define as noise with the characteristics of the noise in the data, and subsequently inverted. Given that the high altitudes of ambiguity for the two interferograms (Table 1) are considerably in excess of the quoted 7 m accuracy of the SRTM DEM used to correct for topographic artefacts [Farr and Kobrick, 2000], we assume the principal source of noise in the data to be phase differences due to

differing levels of water vapor in the troposphere. Water vapor bodies can be spatially continuous over tens of kilometers, and therefore the noise they introduce to the data will be spatially correlated over similar wavelengths (T. J. Wright et al., manuscript in preparation). In order to synthesize realistic noise, therefore, we must first determine the statistical properties of this spatially correlated noise for each interferogram in turn.

[42] Using a far-field area of the interferogram where there is no deformation signal from the earthquake, we estimate a 1-D covariance function for the data by radially averaging a 2-D autocorrelation function calculated using the power spectrum of the data [Hanssen, 2001]. This is valid if the interferogram has been corrected for orbital tilts, as in section 2.1. A curve, of the form $Ae^{-ax} \cos bx$, where x is the separation between two points in the interferogram, A is the maximum variance, and a and b are positive constants, is fitted to this function by standard least squares and can then be used to construct an approximate variance-covariance matrix (VCM) for the noise in the interferogram. For the ascending track interferogram used in this study (Table 1), we find a maximum variance of 20 mm^2 and an e-folding length scale of 18 km for the noise in the far field; for the descending track interferogram (Table 1), the values are 5 mm^2 and 11 km, respectively. Using the VCM for each interferogram we then construct 100 simulations of spatially correlated random noise with which we perturb each of our original data sets. Full details of this method will be given by Wright et al. (manuscript in preparation, 2005).

[43] The 100 perturbed data sets can then be inverted, either by nonlinear optimization [Clarke et al., 1997; Wright et al., 1999] to find the fault geometry, or by a least squares-style inversion for the distribution of slip on the fault plane (Appendix C), to generate a set of 100 model solutions. The distribution of values of each model parameter can be plotted as a histogram, and used to estimate the 1σ uncertainty in that parameter, or plotted against other model parameters and used to qualitatively assess the trade-offs between those parameters (Figures B1 and B2).

[44] As a guide to the interpretation of such trade-off scatterplots and histograms, we consider the single fault case (Figure B1) in detail. The majority of fault parameters (e.g., strike, dip, rake, length and fault location) are well resolved, appearing as tight clusters in the scatterplots and narrow peaks in the histograms, for instance, the X (east) location of the projection of the fault to the surface has an uncertainty of less than 100 m. However, there are trade-offs present between some pairs of parameters, identifiable as positive and/or negative correlations in the scatterplots for those pairs; these can be seen between fault width, slip, fault depth and moment, all parameters that affect the size of the signal that is measured at the surface. Overall, the level of uncertainty is sufficiently small that we can have good confidence in our fault parameter estimates, for instance, that a steeply eastward dipping fault gives the best single fault solution.

Appendix C: Variable Slip Model Inversions

[45] For a fixed fault geometry, the distribution of slip on the fault plane is linearly related to the displacements
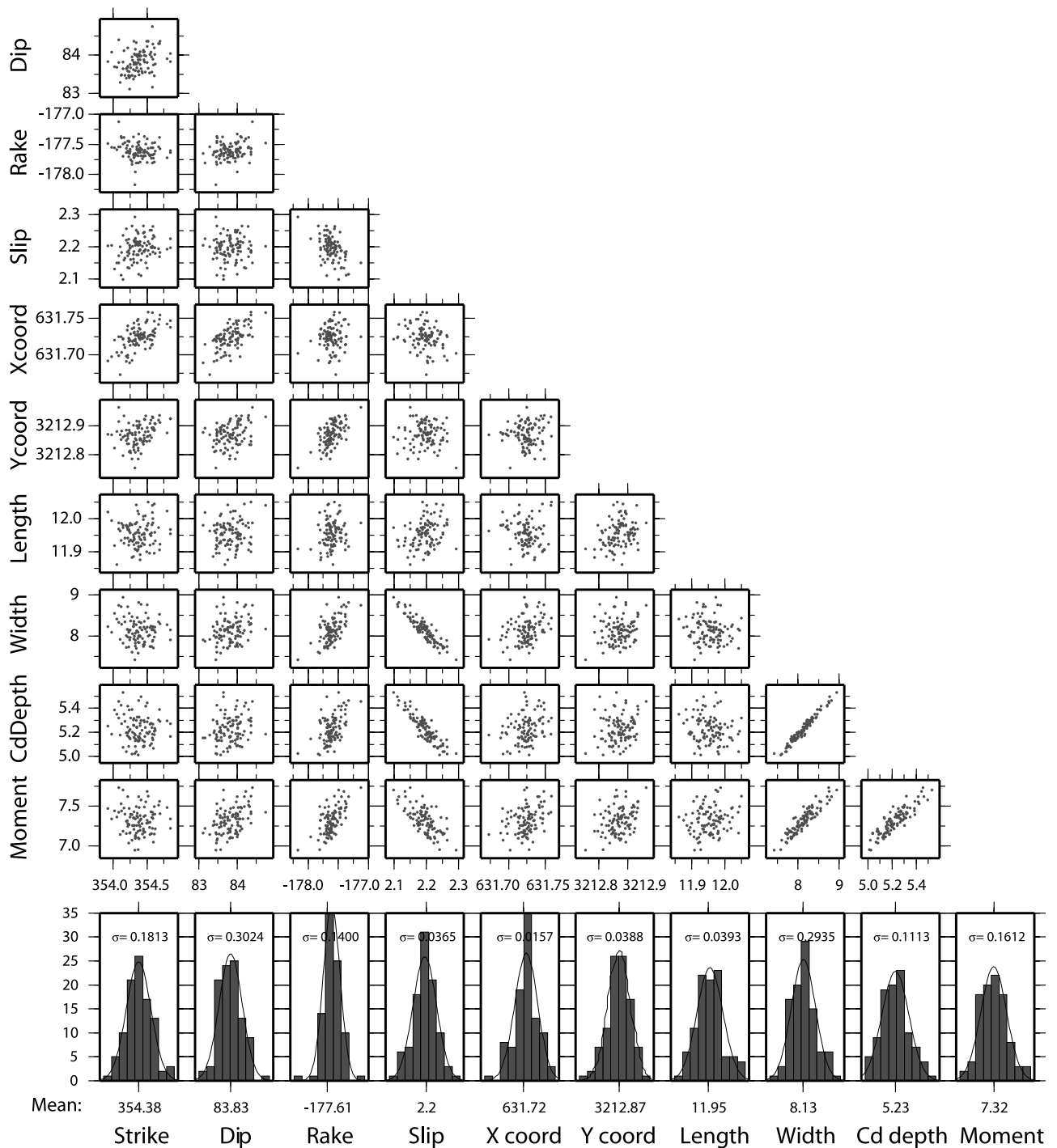
Figure B1. Uncertainties and trade-offs of single fault model parameters computed using Monte Carlo analysis. Histograms show uncertainties in individual model parameters. Scatterplots show degrees of trade-off between pairs of model parameters; positive and negative correlations between pairs of parameters indicate trade-offs between those parameters. (Strike, dip, and rake are in degrees; slip is in m; x and y coordinates (of the center of the fault plane projected updip to the surface) are in UTM km (zone 40); length, width, and centroid (Cd) depth are in km; and moment is in units of 10^{18} N m.)
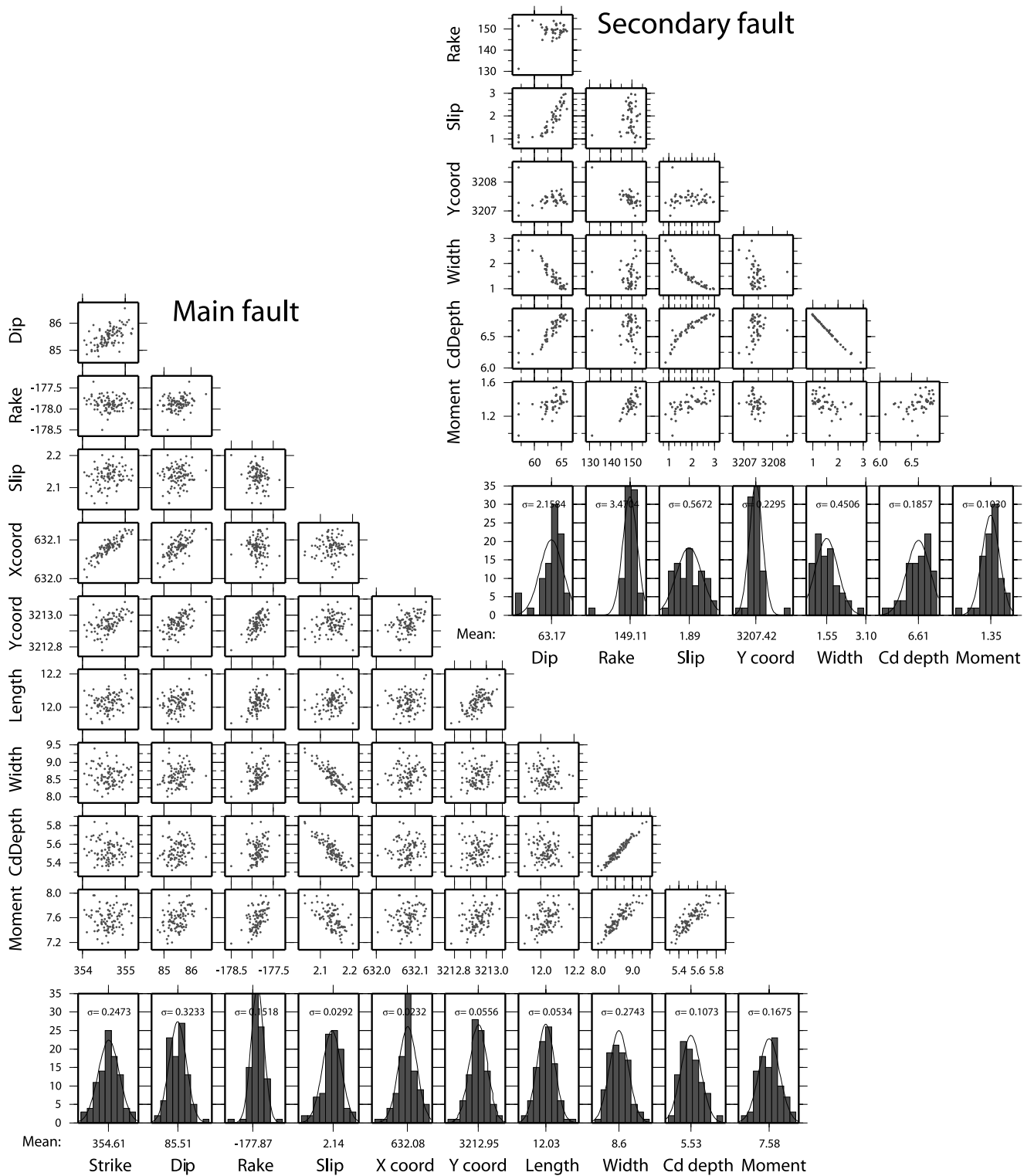
Figure B2. Uncertainties and trade-offs in model parameters for the two fault model. Strike and *x* coordinates are fixed for the secondary fault to prevent the faults from crosscutting. Histograms, scatterplots, and units are as for Figure B1.
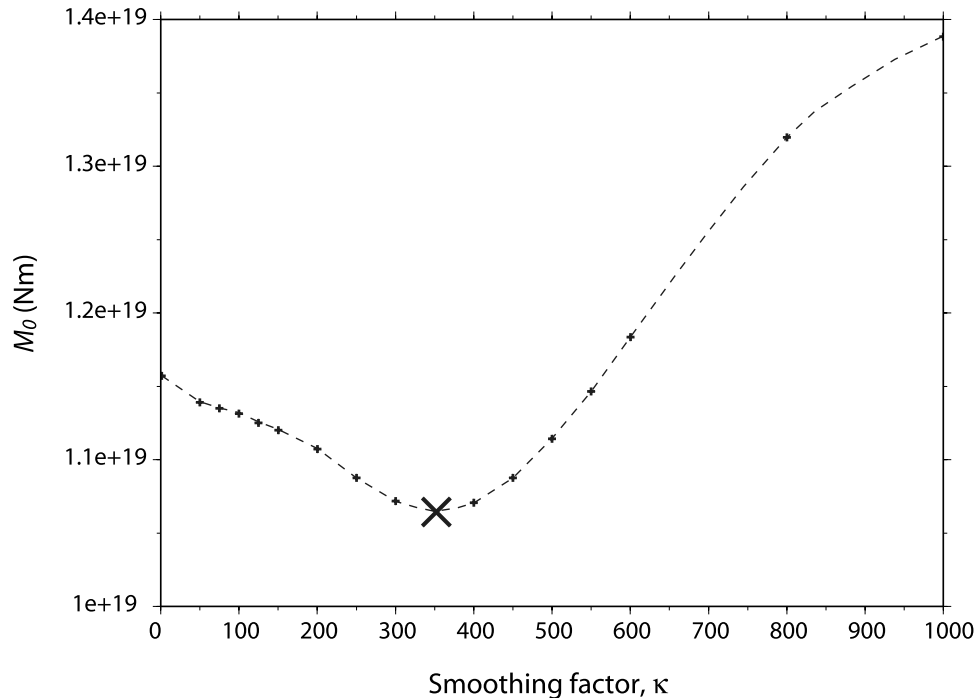
Figure C1. Choice of smoothing parameter for the variable slip model. Each data point on the graph represents a single model run of the variable slip inversion using a different smoothing parameter, and the large cross indicates the value used in our final solution, associated with a minimum in the model seismic moment.

measured by InSAR. For our variable slip inversions, we extend the model fault geometry as described in the text, and subdivide it into 1×1 km patches.

[46] If **m** is a column vector containing the slip on each of the patches on the two faults, and the displacements measured in the ascending track interferogram are given in the column vector $\mathbf{d_a}$, and those from the descending track interferogram by $\mathbf{d_d}$, then we can set up a system of normal equations relating the model to the data:

$$\mathbf{Am} = \mathbf{d}, \tag{C1}$$

where $\mathbf{A}^T = [\mathbf{A_a^T \, A_d^T}]$ and $\mathbf{d}^T = [\mathbf{d_a^T \, d_d^T}]$, $\mathbf{A_a}$ and $\mathbf{A_d}$ being the data kernels relating the slip on each fault patch to the ascending and descending data, respectively, with the rake fixed to the value obtained in the uniform slip inversion. This can be readily modified to solve for variable rake as well as slip (e.g., section 3.1) by changing the matrix **A**, i.e.,

$$\mathbf{A} = \begin{bmatrix} \mathbf{A_{a_h}} & \mathbf{A_{a_v}} \\ \mathbf{A_{d_h}} & \mathbf{A_{d_v}} \end{bmatrix}, \tag{C2}$$

where the h and v suffices here refer to data kernels and corresponding model parameters calculated for pure "horizontal" (strike-slip) and "vertical" (dip-slip) displacement, respectively. In this case, $\mathbf{m}^T = [\mathbf{m_h^T \, m_v^T}]$, where $\mathbf{m_h}$ is a vector containing the amount of strike-slip motion for each fault patch, and $\mathbf{m_v}$ likewise the dip-slip motion.

[47] We assume here that orbital tilts and offsets, which would otherwise contribute to the measured displacements, have already been removed by postprocessing the data (see section 2.1). In order to prevent unphysical oscillatory slip, a Laplacian smoothing condition is imposed whereby the sum of the partial second differentials of slip in the along-strike and downdip directions is minimized for the slip on each fault patch. Including the smoothing in our system of equations gives

$$\mathbf{A_s m} = \mathbf{d'}, \tag{C3}$$

where

$$\mathbf{A_s} = \begin{bmatrix} \mathbf{A} \\ \kappa \nabla^2 \end{bmatrix}, \tag{C4}$$

Figure C2. Resolution of the variable slip model. (a) Plot of resolution length scale ρ for our preferred model ($\kappa = 350$). (b) Pattern of slip obtained when the data are inverted with $\kappa = 350$. The principal features of the slip pattern have length scales shorter than ρ for those locations. (c) Plot of 1σ uncertainties in the slip values where $\kappa = 350$, estimated using Monte Carlo analysis. Uncertainties are very low on both faults. (d) Plot of ρ for a model with lower smoothing ($\kappa = 75$). Values are over 50% lower than at the equivalent locations in Figure C2a, indicating an improvement in resolution. (e) Slip model obtained with $\kappa = 75$. Slip pattern is rough, with high strain gradients, large maxima of slip, and a deep patch of slip on the main fault. (f) Plot of 1σ uncertainties in the slip values where $\kappa = 75$, estimated using Monte Carlo analysis. Uncertainties are up to 5 times greater than for the preferred model. Contours are omitted in areas of the highest gradients.
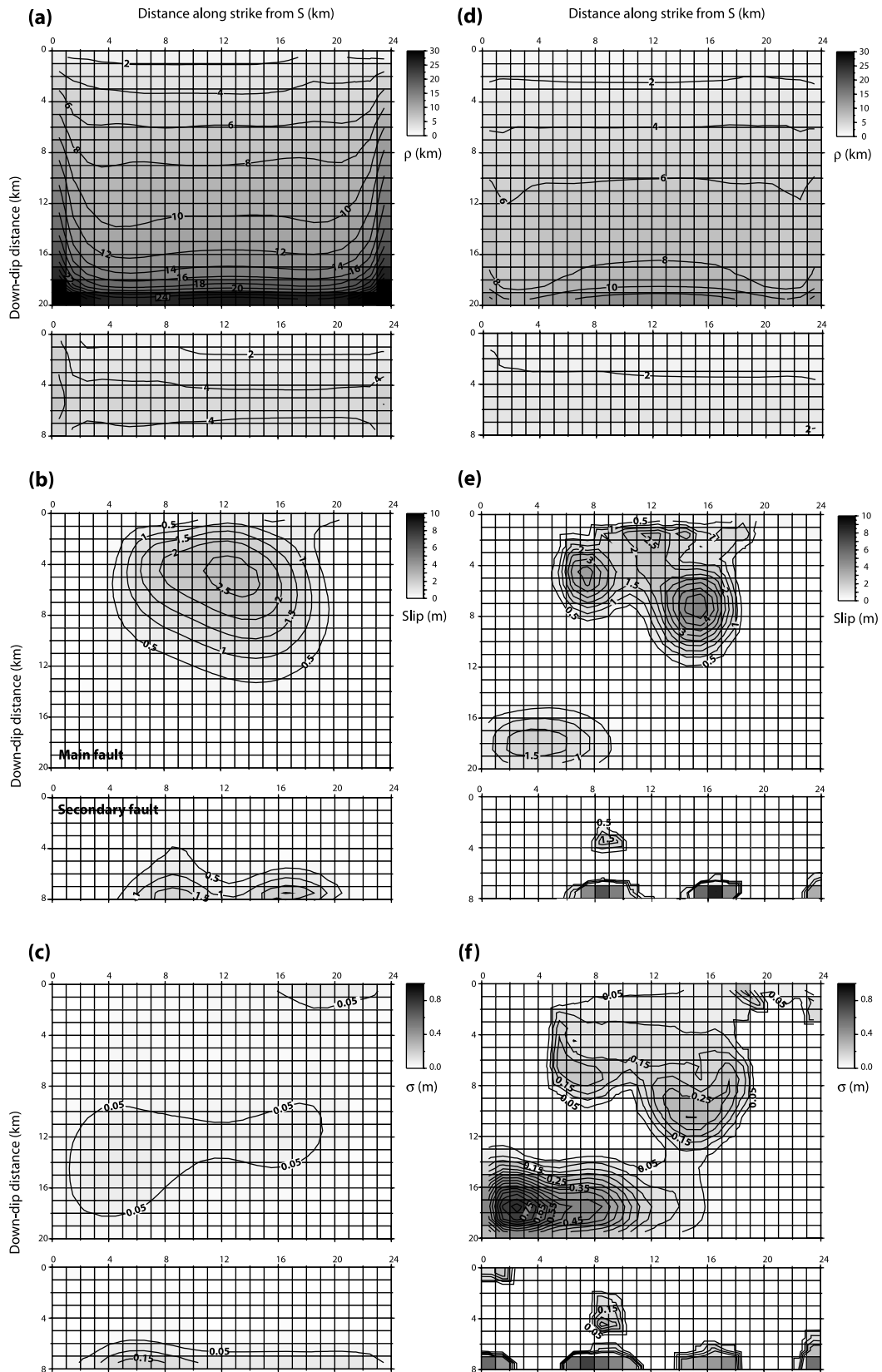
Figure C2

$$\mathbf{d}' = \begin{bmatrix} \mathbf{d} \\ \mathbf{0} \end{bmatrix}, \qquad (C5)$$

∇^2 is the finite difference approximation of the Laplacian operator, and κ is a scalar smoothing factor used to weight the smoothing in the inversion. We solve equation (C3) in the fixed rake case using fast nonnegative least squares [*Bro and De Jong*, 1997], so that only positive (right-lateral) slip is allowed, and in the variable rake case with a unconstrained least squares method, so as to allow upward and downward vertical motions. It is assumed that slip is zero beyond the boundaries of the fault.

[48] In a variable slip inversion, the choice of smoothing parameter, κ, can greatly affect the resulting slip distribution. For our preferred two-fault model, we choose a value of κ that minimizes the seismic moment, M_0, having systematically varied κ for a series of re-runs of the inversion (Figure C1). In this case, we believe that the value selected, $\kappa = 350$, reflects a compromise between eradicating spurious patches of deep slip on the main fault through a sufficiently high level of smoothing, and not imposing high slip on areas of the fault which do not require it through over smoothing.

[49] To assess the degree of detail that it is possible to resolve with this level of smoothing, we calculate the resolution matrix for the model given by

$$\mathbf{R} = \left[\mathbf{A_s}^T \mathbf{A_s}\right]^{-1} \mathbf{A}^T \mathbf{A}. \qquad (C6)$$

The elements of $\mathbf{R}$ range between 0 and 1. If the model is perfectly resolved, $\mathbf{R}$ will be an identity matrix; if certain model parameters are underdetermined, the corresponding term on the leading diagonal of $\mathbf{R}$ will be less than 1 and there will be off-diagonal terms. As the leading diagonal terms of $\mathbf{R}$ reflect the degree at which the slip on a given patch is averaged in the model with the values for the patches surrounding it, we use them to generate a proxy for the linear dimension of resolution of the model. If $\mathbf{r} = (r_1 \ r_2 \ \ldots \ r_i \ \ldots \ r_M)^T$ is a vector containing the diagonal terms of $\mathbf{R}$, where M is the number of fault parameters, and given a fault patch area of 1 km^2, then we define the linear dimension of resolution, ρ, for the ith fault patch, as

$$\rho_i = \frac{1}{\sqrt{r_i}}. \qquad (C7)$$

The values of ρ are plotted in Figure C2. In general, the resolution degrades steadily with depth on the main fault, with good resolution at the surface ($\rho < 2$ km) and poor resolution at the ends and base of the fault ($\rho > 20$ km); resolution is higher ($\rho < 4$ km) on the secondary fault. At depths corresponding to the region of peak slip on the main fault (~ 5 km), $\rho \approx 5$ km, still sufficient to resolve a region of slip greater than 2 m on the fault; at depths below 12 km, $\rho > 10$ km, and features will be poorly resolved (Figure C2a). Since the main slip features on the main and secondary faults occur above this depth (Figure C2b), we therefore believe they can be resolved in our model.

[50] Resolution can be improved by reducing the level of smoothing, as can be seen if a plot of ρ is made where $\kappa = 75$ (Figure C2d). Values of ρ are generally 50% lower on the main fault and 100% lower on the secondary fault than for our preferred model (Figure C2a). The model solution corresponding to $\kappa = 75$ is plotted in Figure C2e, and is considerably rougher than our preferred model (Figure C2b), with multiple slip features on both faults. The maxima of slip are extreme in this case, 4.9 m on the main fault and 9.5 m on the secondary fault, and there is a broad patch of slip at depths of 16–20 km on the main fault. We believe that, given the high uncertainties associated with these features (Figure C2f) and given that the high strain gradients on the fault implied by the large slip values are not physically reasonable, the rougher model is not an accurate representation of the earthquake source. It is well known [e.g., *Backus and Gilbert*, 1970] that model accuracy and resolution have a reciprocal relationship. Here we prefer a model with lower resolution than is possible with these data, but which we believe is more likely to be accurate.

References

Ambraseys, N., and C. Melville (1982), *A History of Persian Earthquakes*, Cambridge Univ. Press, New York.

Backus, G., and F. Gilbert (1970), Uniqueness in the resolving power of gross Earth data, *Philos. Trans. R. Soc. London, Ser. A*, 266, 123–192.

Berberian, M. (1976), Contribution to the seismotectonics of Iran, part II, Materials for the study of the seismotectonics of Iran, *Rep. 39*, Geol. Surv. of Iran, Tehran.

Berberian, M., and M. Qorashi (1994), Coseismic fault-related folding during the south Golbaf earthquake of November 20, 1989, in southeast Iran, *Geology*, 22, 531–534.

Berberian, M., J. Jackson, M. Qorashi, and M. Kadjar (1984), Field and teleseismic observations of the 1981 Golbaf-Sirch earthquakes in SE Iran, *Geophys. J. R. Astron. Soc.*, 77, 809–838.

Berberian, M., C. Baker, E. Fielding, J. Jackson, B. Parsons, K. Priestley, M. Qorashi, M. Talebian, R. Walker, and T. Wright (2001), The 14 March 1998 Fandoqa earthquake (M_w 6.6) in Kerman province, S.E. Iran: Re-rupture of the 1981 Sirch earthquake fault, triggering of slip on adjacent thrusts, and the active tectonics of the Gowk fault zone, *Geophys. J. Int.*, 146, 371–398.

Bro, R., and S. De Jong (1997), A fast non-negativity-constrained least squares algorithm, *J. Chemometr.*, 11, 392–401.

Bürgmann, R., P. Rosen, and E. Fielding (2000), Synthetic Aperture Radar interferometry to measure Earth's surface topography and its deformation, *Annu. Rev. Earth. Planet. Sci.*, 28, 169–209.

Chu, D. Z., and R. G. Gordon (1998), Current plate motions across the Red Sea, *Geophys. J. Int.*, 135, 313–328.

Clarke, P., D. Paradissis, P. Briole, P. England, B. Parsons, H. Billiris, G. Veis, and J.-C. Ruegg (1997), Geodetic investigation of the 13 May 1995 Kozani-Grevena (Greece) earthquake, *Geophys. Res. Lett.*, 24(6), 707–710.

DeMets, C., R. Gordon, D. Argus, and S. Stein (1994), The effect of recent revisions to the geomagnetic reversal time scale on estimates of current plate motions, *Geophys. Res. Lett.*, 21(20), 2191–2194.

Eberhart-Phillips, D., et al. (2003), The 2002 Denali fault earthquake, Alaska: A large magnitude, slip-partitioned event, *Science*, 300, 1113–1118.

Engdahl, E. R., R. van der Hilst, and R. Buland (1998), Global teleseismic earthquake relocation with improved travel times and procedures for depth determination, *Bull. Seismol. Soc. Am.*, 88, 722–743.

Farr, T., and M. Kobrick (2000), Shuttle Radar Topography Mission produces a wealth of data, *Eos Trans. AGU*, *81*, 583, 585.

Fialko, Y. (2004), Probing the mechanical properties of seismically active crust with space geodesy: Study of the coseismic deformation due to the 1992 M_w 7.3 Landers (southern California) earthquake, *J. Geophys. Res.*, *109*, B03307, doi:10.1029/2003JB002756.

Fialko, Y., M. Simons, and D. Agnew (2001), The complete (3-D) surface displacement field in the epicentral area of the 1999 M_w 7.1 Hector Mine earthquake, California, from space geodetic observations, *Geophys. Res. Lett.*, *28*(16), 3063–3066.

Fielding, E. J., T. J. Wright, J. Muller, B. Parsons, and R. Walker (2004), Aseismic deformation of a fold-and-thrust belt imaged by SAR interferometry near Shahdad, SE Iran, *Geology*, *32*, 577–580.

Fielding, E. J., M. Talebian, P. A. Rosen, H. Nazari, J. A. Jackson, M. Ghorashi, and R. Walker (2005), Surface ruptures and building damage of the 2003 Bam, Iran, earthquake mapped by satellite synthetic aperture radar interferometric correlation, *J. Geophys. Res.*, *110*, B03302, doi:10.1029/2004JB003299.

Hanssen, R. (2001), *Radar Interferometry: Data Interpretation and Error Analysis*, Springer, New York.

Jónsson, S., H. Zebker, P. Segall, and F. Amelung (2002), Fault slip distribution of the 1999 M_w 7.1 Hector Mine earthquake, California, estimated from satellite radar and GPS measurements, *Bull. Seismol. Soc. Am.*, *92*(4), 1377–1389.

Kurushin, R. A., A. Bayasgalan, M. Ölziybat, B. Enhtuvshin, P. Molnar, C. Bayarsayhan, K. W. Hudnut, and J. Lin (1997), *The Surface Rupture of the 1957 Gobi-Altay, Mongolia, Earthquake*, Spec. Pap. Geol. Soc. Am., *320*, 143 pp.

Massonnet, D., and K. L. Feigl (1998), Radar interferometry and its application to changes in the Earth's surface, *Rev. Geophys.*, *36*(4), 441–500.

Michel, R., J.-P. Avouac, and J. Taboury (1999), Measuring ground displacements from SAR amplitude images: Application to the Landers earthquake, *Geophys. Res. Lett.*, *26*, 875–878.

Okada, Y. (1985), Surface deformation due to shear and tensile faults in a half-space, *Bull. Seismol. Soc. Am.*, *75*(4), 1135–1154.

Peltzer, G., F. Crampé, and G. King (1999), Evidence of nonlinear elasticity of the crust from the M_w 7.6 Manyi (Tibet) earthquake, *Science*, *286*, 272–276.

Rosen, P. A., S. Hensley, G. Peltzer, and M. Simons (2004), Updated Repeat Orbit Interferometry package released, *Eos Trans. AGU*, *85*(5), 35.

Sella, G. F., T. H. Dixon, and A. Mao (2002), REVEL: A model for Recent plate velocities from space geodesy, *J. Geophys. Res.*, *107*(B4), 2081, doi:10.1029/2000JB000033.

Simons, M., Y. Fialko, and L. Rivera (2002), Coseismic deformation from the 1999 M_w 7.1 Hector Mine, California earthquake as inferred from InSAR and GPS observations, *Bull. Seismol. Soc. Am.*, *92*, 1390–1402.

Talebian, M., et al. (2004), The 2003 Bam (Iran) earthquake: Rupture of a blind strike-slip fault, *Geophys. Res. Lett.*, *31*, L11611, doi:10.1029/2004GL020058.

Tatar, M., D. Javan, A. Farabhod, A. Paul, and D. Hatzfeld (2004), Aftershock seismicity of the Bam earthquake (abstract), *Geophys. Res. Abstr.*, *6*, 07893.

Vernant, P., et al. (2004), Present-day crustal deformation and plate kinematics in the Middle East constrained by GPS measurements in Iran and northern Oman, *Geophys. J. Int.*, *157*, 381–398.

Walker, R., and J. A. Jackson (2002), Offset and evolution of the Gowk Fault, S.E. Iran: A major intra-continental strike-slip system, *J. Struct. Geol.*, *24*, 1677–1698.

Wessel, P., and W. H. F. Smith (1998), New, improved version of generic mapping tools released, *Eos Trans. AGU*, *79*, 579.

Wright, T. J., B. Parsons, J. Jackson, M. Haynes, E. Fielding, P. England, and P. Clarke (1999), Source parameters of the 1 October 1995 Dinar (Turkey) earthquake from SAR interferometry and seismic bodywave modelling, *Earth Planet. Sci. Lett.*, *172*, 23–37.

Wright, T. J., Z. Lu, and C. Wicks (2003), Source model for the M_w 6.7, 23 October 2002, Nenana Mountain Earthquake (Alaska) from InSAR, *Geophys. Res. Lett.*, *30*(18), 1974, doi:10.1029/2003GL018014.

Wright, T. J., Z. Lu, and C. Wicks (2004a), Constraining the slip distribution and fault geometry of the M_w 7.9, 3 November 3 2002, Denali Fault earthquake with InSAR and GPS, *Bull. Seismol. Soc. Am.*, *94*(6B), S175–S189.

Wright, T. J., B. E. Parsons, and Z. Lu (2004b), Toward mapping surface deformation in three dimensions using InSAR, *Geophys. Res. Lett.*, *31*, L01607, doi:10.1029/2003GL018827.

————————————

E. J. Fielding, Jet Propulsion Laboratory, California Institute of Technology, 4800 Oak Grove Drive, Pasadena, CA 91109, USA.

G. J. Funning, Berkeley Seismological Laboratory, University of California, 215 McCone Hall, Berkeley, CA 94720-4760, USA. (gareth@seismo.berkeley.edu)

J. A. Jackson, COMET, Bullard Laboratories, University of Cambridge, Madingley Road, Cambridge CB2 0EZ, UK.

B. Parsons and T. J. Wright, COMET, Department of Earth Sciences, University of Oxford, Parks Road, Oxford OX1 3PR, UK.